Evaluating the subsidence above gas reservoirs with an elasto-viscoplastic constitutive law. Laboratory evidences and case histories

(Article begins on next page)

20 April 2024

1   Date paper revised: September 10th, 2020

2   To be submitted to

3   Geomechanics for Energy and the Environment:

4   **Evaluating the subsidence above gas reservoirs with an elasto-**

5   **viscoplastic constitutive law: laboratory evidences and case histories**

6   G. Musso[a,*], G. Volonté[b], F. Gemelli[c], A. Corradi[c],

7   S.K. Nguyen[a,d], R. Lancellotta[a], M. Brignoli[c] and S. Mantica[c]

8

9   a - Department of Structural, Building and Geotechnical Engineering, Politecnico di Torino, corso

10   Duca degli Abruzzi 24, 10129 Torino, ITALY.

11   b - Department of Petroleum R&D, Eni S.p.A., Via Maritano 26, 20097 San Donato Milanese,

12   ITALY.

13   c - Department of EOR Technologies and Geomechanics, Eni S.p.A., Via Emilia 1, 20097 San Donato

14   Milanese, ITALY.

15   d - Department of Mechanics of Structure and Materials, Institut Supérieur de l'Aéronautique et de

16   l'Espace (ISAE), Avenue Édouard-Belin 10, 31055 Toulouse, FRANCE.

17

18   *corresponding author guido.musso@polito.it

19

20

21 **Abstract**

22

23 Reliable modelling of subsidence is an important objective for companies and regulators interested in safe and

24 environmentally sustainable development of hydrocarbon fields. Subsidence is triggered by the depletion of reservoirs

25 and connected aquifers, which causes the compaction of the geologic layers. A fundamental requirement of models is the

26 correct prediction of the pore pressure changes taking place during the production; but capturing the mechanical

27 behaviour of the reservoir material and its proper constitutive modelling are equally important. In some cases, the geologic

28 materials show a time-dependent (viscous) behaviour, which might lead to creep strains at constant stress conditions. As

29 a consequence, subsidence might be delayed with respect to hydrocarbon production, or continue even when production

30 has stopped.

31 This paper refers to the case of two gas reservoirs from the Adriatic basin. Numerical simulations based on elasto-plastic

32 constitutive models, even if relying on very accurate reconstructions of the pore pressure histories, did not provide a

33 satisfactory match of subsidence history. This motivated a further insight into the time-dependent behaviour of the sandy

34 reservoir materials. The results of an exhaustive laboratory investigation were interpreted in light of an existing elasto-

35 viscoplastic model, recently implemented by the authors in a commercial Finite Element code. Numerical predictions are

36 compared to field data, which include both measurements of compaction, taken in the reservoirs with radioactive markers,

37 and surface settlements recorded with GPS and bathymetric surveys. A very good agreement was obtained between

38 simulation results and field data, in terms of maximum settlements, settlement history and extent of the subsidence bowl.

39 **Keywords:**

40 Subsidence; time-dependent mechanical behaviour; creep; elasto-viscoplastic constitutive law; gas reservoir; case

41 history

42

1. Introduction

Land subsidence is a potential undesired effect of underground fluid extraction, which in some cases can seriously affect the environment and human activities. Subsidence can increase the risk of flooding along coastal and estuarine areas, as in New Orleans with the Katrina Hurricane[1] and in Bangkok in 2011[2]. In extreme cases, anthropic subsidence can cause the ground floor to sink below the water level, which in proximity of populated or environmentally relevant lands can impact on social or ecological equilibria[3], requiring the building of new dykes (see e.g. Refs. 4, 5) or rising the height of old ones[6]. In offshore fields, subsidence due to hydrocarbon extraction can reduce the air gap between the lower platforms deck and the sea, exposing platforms to waves inundation and requiring very costly extraordinary maintenance to keep the production activities ongoing[7]. Both regulators and energy companies are then deeply interested in reliable predictive models, which allow foreseeing the magnitude and extent of the ground settlements, ultimately leading to early implementation of mitigation strategies whenever necessary.

Factors that can lead to appreciable subsidence are highly compressible reservoir rocks, considerable decrease of pore pressure during hydrocarbon production, thick or shallow reservoirs and low contrast between the stiffness of the reservoir and that of the overburden[8].

Saturated soils and rocks have a coupled hydro-mechanical behaviour and, in principle, both the flow and the mechanical problems should be solved simultaneously through coupled hydro-mechanical analyses. This is seldom done, because of the demanding numerical issues and computational efforts required for large scale problems such as the one under consideration (e.g. Ref. 9). However, for gas reservoirs, very little hydro-mechanical coupling is expected because the pore fluid has a very high compressibility compared to the rock. A one-way coupling procedure, where the pore pressure distribution at different times is first estimated by means of reservoir fluid dynamic simulations and then used to simulate the mechanical response, is accepted in these cases, provided that the mechanical characterization of reservoir rocks is consistent in both flow and mechanical models. The first mathematical model for the prediction of subsidence was formulated by Geertsma[10] on the basis of the 'strain nuclei' approach. This model considers the subsurface as a poro-elastic half space, and it provides the analytical solution of the displacement caused by the pore pressure drop occurring within a material point (nucleus of strain) having some specific coordinates. The analytical solution can be readily extended to real cases by discretizing the reservoir with a proper number of grid blocks (strain nuclei) and integrating the effects of the pressure decrease of each grid block over the whole reservoir, thus predicting the subsidence bowl due to the development of the field. The solution for the simplified case of an axisymmetric disc-shaped reservoir with a uniform pressure can be found in Geertsma[11].

The Geertsma model introduces the very stringent assumptions of a homogeneous material with a linear isotropic elastic behaviour. Other analytical models (see e.g. Refs. 12, 13) relaxed the homogeneity and the isotropy assumptions, while maintaining linear elasticity. However, it is well known that the mechanical behaviour of most of the geologic materials is elastic only at very small strains, and that it is generally not linear.

A significant improvement in subsidence modelling was obtained accounting for plastic strains occurring along compression stress paths, by implementing volumetric hardening elasto-plastic models such as the Modified Cam Clay Model[14] into Finite Element (FE) codes. Simulations based on these models proved to be satisfactory for several field cases[15-17], but failed in detecting the correct values and trends of subsidence for others[18-21], where an increase in subsidence was appreciated even after production had stopped or reduced significantly.

Two major mechanisms are considered to be responsible for the delayed subsidence and for the discrepancy between the simulations and field measurements. The first one is the delayed depletion of low permeability layers, such as shales or clays, both within and outside the reservoir (see e.g. Ref. 22). Pore pressure decrease, originating in the gas bearing layers, diffuses very slowly through shales or clays, because of their low permeability. As such, shale compaction will continue after suspending or even stopping production. Such a compaction adds up to the one of the reservoir and induces a delayed increase of subsidence, which can be observed only in later stages of the productive life of the field. However, delayed subsidence has been observed also in the first years of production, without any relationship to stop of production[23].

Delayed subsidence might also depend on the time-dependent behaviour of the materials. For soils, volume strains are well known to increase with time even under a constant effective stress, a creep phenomenon known as secondary compression[24,25]. A similar behaviour has been observed with reservoir sands[26] and shales[27] loaded to high effective stresses. Chang et al.[20] studied the subsidence history of onshore gas fields by summing the elastic subsidence of a disc-shaped reservoir (evaluated according to Geertsma[11]) to the compaction of the shale layers surrounding the reservoir. The hydraulic behaviour of the shales was modelled with the one-dimensional diffusion equation whereas the mechanical behaviour was modelled with a one-dimensional viscoplastic law. Notwithstanding the simplifying assumptions, introduced both with respect to the geometry and the hydro-mechanical behaviour, they obtained a good qualitative match of the subsidence history, suggesting that creep and delayed depressurization of shales are key aspects to be taken into account for the improvement of subsidence predictions (see also Ref. 28).

This paper aims at discussing the impact of the time-dependent behaviour of reservoir sands on the subsidence of gas fields. After briefly introducing some elasto-viscoplastic models of use for soils and rocks, the main results of a laboratory investigation on the time-dependent behaviour of sands from two reservoirs of the Adriatic basin are provided. The

4

101 adequacy of the elasto-viscoplastic model of Vermeer and Neher[29] (VNM in the following) in reproducing the laboratory

102 results is discussed, justifying its implementation into a commercial FE code. Laboratory tests served also to determine

103 the VNM parameters to be used for the numerical simulations of the subsidence of the two fields. The pressure history

104 and related compaction of clay layers were taken into account in the simulations where appropriate. Model predictions

105 are finally compared to real field data, based upon the extensive subsidence and compaction monitoring campaigns

106 performed.

107

108   **2.   Elasto-viscoplastic models for soils and reservoir rocks**

109 Several models have been formulated in past years to reproduce the time-dependent behaviour of soils and rocks (see e.g.

110 Ref. 30) and both viscoelastic and viscoplastic relationships have been proposed. Elasto-plastic laws with volumetric

111 hardening are currently used by the oil industry for geomechanical simulations. Elasto-viscoplastic models can be seen

112 as an enhancement of elasto-plastic ones. It is then of interest to check their performance in subsidence prediction, since

113 they might ensure an improvement in the cases where the ones obtained using elasto-plasticity are not accurate enough.

114 A brief description of the families of constitutive models which enhance hardening plasticity to account for time-

115 dependent behaviour, with special reference to elasto-viscoplastic models with volumetric hardening, is given below.

116 These models share the assumption that the total strain can be decomposed into the sum of an elastic and of a viscoplastic

117 component:

118
$$\boldsymbol{\varepsilon} = \boldsymbol{\varepsilon}^{e} + \boldsymbol{\varepsilon}^{vp} \tag{1}$$

119 where $\boldsymbol{\varepsilon}$ is the small strain tensor, while $\boldsymbol{\varepsilon}^{e}$ and $\boldsymbol{\varepsilon}^{vp}$ are its elastic and viscoplastic components.

120 The elastic strains are time independent and they are related to stress increments through some generalized Hooke's law.

121 Viscoplastic strains are time-dependent, and they are usually evaluated either in the frame of the theory of the Non

122 Stationary Flow Surface (NSFS) or in the frame of the Overstress Theory.

123

124 *2.1 Models formulated in the frame of the Non Stationary Flow Surface*

125 The theory of the Non Stationary Flow Surface has been originally developed by Naghdi and Murch[31] and by Olszak and

126 Perzyna[32] and it is based on the assumption that the yield surface evolves with time, even when the stress is constant.

127 In volumetric hardening plasticity, the yield function has the expression:

$$f = f\left(\boldsymbol{\sigma}', p'_{c}(\boldsymbol{\varepsilon}^{p}, \gamma)\right) \tag{2}$$

where $\boldsymbol{\sigma}$' is the effective stress tensor and p'_{c} is the hardening parameter, related to the plastic strain tensor $\boldsymbol{\varepsilon}^{p}$ and, where required, to other variables γ accounting for effects such as grain bonding, saturation, temperature, chemical composition of the pore fluid, etc. In the NSFS models, the yield function depends on the same variables used in elastic-hardening models, but it also depends on some time-dependent function β:

$$f = f\left(\boldsymbol{\sigma}', p'_{c}(\boldsymbol{\varepsilon}^{vp}, \gamma), \beta\right) \tag{3}$$

The effect of time is often introduced through the viscoplastic strain rate $\dot{\boldsymbol{\varepsilon}}^{vp}$ and specifically imposing that the hardening parameter depends both on the viscoplastic strain and on the viscoplastic strain rate:

$$p'_{c} = p'_{c}(\boldsymbol{\varepsilon}^{vp}, \dot{\boldsymbol{\varepsilon}}^{vp}, \gamma) \tag{4}$$

Equation 4 is consistent with the isotach concept proposed by Šuklje[33], which states that the state of a volume of soil can be described by a single $(p', e, \dot{e})$ relationship, where p' is the mean effective stress, e and $\dot{e}$ are the void ratio and the rate at which it changes. Under the hypothesis of incompressible solid grains, the volume strain is

$$\varepsilon_{v} = -\frac{\Delta e}{1+e_0} \tag{5}$$

where Δe is the change in void ratio and e_0 is the void ratio at some reference conditions. The isotach concept implies then that the position of the Normal Compression Line (describing first time compression of the soil volume) in the compression plane (p', e) depends on the applied strain rate: first time compressions at different strain rates are described by different Normal Compression Lines. During a creep phase, the stress remains constant and the strains increase but their velocity decreases with time. Therefore, as remarked by De Gennaro and Pereira[34] "soils may experience both compression under constant strain rate (i.e. following a rate-line) or delayed compression under sustained constant load (i.e. decreasing the strain rate and crossing multiple rate-lines)" (see Fig. 1). The yield stress increases then with the strain rate (see e.g. Ref. 35).
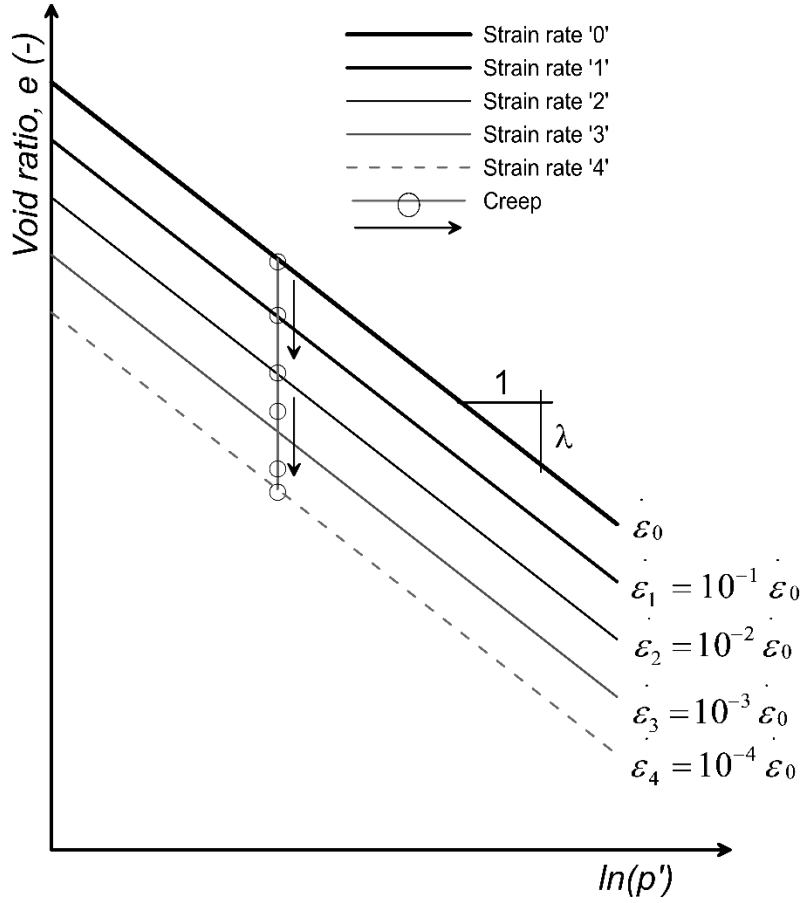
Fig. 1. Isotach concept: Normal Compression Lines at different constant strain rates are parallel lines on the compression plane. During a creep process the stress remains constant while the volume decreases at decreasing rates, thus crossing the NCL of different strain rates

de Waal and Smits[36] presented results of one-dimensional compression of sandstones, interpreted with a stress rate dependent model, which have been also reproduced with a strain rate NSFS model by Cassiani et al.[37]. By introducing the assumptions of eq. (4) into eq. (3), it follows:

$$f = f(\sigma', p'_c(\varepsilon^{vp}, \dot{\varepsilon}^{vp}, \gamma)) \tag{6}$$

The yield function f of the Modified Cam Clay Model:

$$f = q^2 - M^2 p'(p'_c - p') \tag{7}$$

is usually adopted (see e.g. Refs 37-38). In (7) q is the deviatoric stress and M the slope of the critical state line in the p', q plane:

$$p' = \tfrac{1}{3}\sigma'_{ii}, \quad q = \sqrt{3}\sqrt{J_2}, \qquad J_2 = \tfrac{1}{2}s_{ij}s_{ij} \qquad s_{ij} = \sigma'_{ij} - p'\delta_{ij} \quad M = \frac{6\sin\phi'_{cv}}{3 - \sin\phi'_{cv}} \tag{8}$$

7

163   with ϕ'_{cv} friction angle at constant volume conditions.

164   A NSFS model for unsaturated conditions, relying of the yield and plastic potential functions of the Barcelona Basic

165   Model[39], is discussed in Ref. 34.

166   The infinitesimal increment of viscoplastic strains $d\boldsymbol{\varepsilon}^{vp}$ is given by:

167
$$d\boldsymbol{\varepsilon}^{vp} = \Lambda \frac{\partial g}{\partial \boldsymbol{\sigma}'} \tag{9}$$

168   where g is the plastic potential function and Λ the plastic multiplier. As in hardening plasticity, the stress state is not

169   allowed outside of the yield surface and the constraint $f \leq 0$ applies. Very often an associated flow rule is assumed and

170    $f = g$.

171   The value of Λ is then determined by introducing eq. (9) into the consistency condition $df = 0$:

172
$$df = \frac{\partial f}{\partial \boldsymbol{\sigma}'} : d\boldsymbol{\sigma}' + \frac{\partial f}{\partial \alpha} d\alpha + \frac{\partial f}{\partial p'_c}\left(\frac{\partial p'_c}{\partial \varepsilon_v^{vp}} d\varepsilon_v^{vp} + \frac{\partial p'_c}{\partial \dot{\varepsilon}_v} d\dot{\varepsilon}_v\right) = 0 \tag{10}$$

173   In eq. (10), the two hardening mechanisms are made evident. The first one is related to the magnitude of the viscoplastic

174   volume strain, and it is usually assumed to be the same of the Modified Cam Clay Model:

175
$$\frac{\partial p'_c}{\partial \varepsilon_v^{vp}} = \frac{1+e_0}{\lambda - \kappa} p'_c \tag{11}$$

176   where λ is the elasto-viscoplastic logarithmic compliance and κ is the elastic logarithmic compliance, defined in terms of

177   void ratio. The second hardening mechanism is related to the strain rate, which is usually expressed by a power law

178   relating p'_c to $\dot{\varepsilon}_v$.

179

180   *2.2 Models formulated in the frame of the Overstress Theory*

181   The Overstress Theory was originally developed by Malvern[40] for one-dimensional conditions and extended to the three-

182   dimensional case by Perzyna[41,42] and Olszak and Perzyna [32]. It requires a static yield surface f_s , which separates the non-

183   viscous regime from the viscoplastic regime, thus defining the size of the purely elastic domain, and a dynamic loading

184   surface f_d, related to the current stress state. The Overstress Theory aims at predicting the strain rates, decomposed into

185   elastic and viscoplastic components:

186
$$\dot{\boldsymbol{\varepsilon}} = \dot{\boldsymbol{\varepsilon}}^e + \dot{\boldsymbol{\varepsilon}}^{vp} \tag{12}$$

8

187 The stress state can be within, on, or outside the static yield surface f_s and the consistency condition does not apply. The

188 viscoplastic strain rate $\dot{\boldsymbol{\varepsilon}}^{vp}$ is then given by a flow rule with respect to the dynamic loading surface f_d:

189
$$\dot{\boldsymbol{\varepsilon}}^{vp} = \mu \langle \phi(F) \rangle \frac{\partial f_d}{\partial \boldsymbol{\sigma'}} \tag{13}$$

190 where μ is a fluidity parameter and $\phi(F)$ is the overstress function, expressing the distance between f_d and f_s. According

191 to the original Overstress Theory:

192
$$\langle \phi(F) \rangle = \begin{cases} 0 & if \ \ F \leq 0 \\ \phi(F) & if \ \ F > 0 \end{cases} \tag{14}$$

193 with F > 0, F<0, and F =0 when the state of stress P is outside, within, or on f_s[30].

194 Determination of the static yield surface is problematic: experimental studies generally remarked the dependency of the

195 yield stress on the strain (or loading) rate, but there are no experimental data proving the existence of a threshold rate

196 below which the yield surface does not depend on the rate anymore[43]. To overcome this issue, recent models ('Extended

197 Overstress Theory') adopt a reference yield surface f_r (Fig. 2) instead of the static yield surface f_s, and viscoplastic strains

198 are anticipated also for F< 0[29,44-46]. Equation (12) is then replaced by expressions such as[41]:

199
$$\dot{\boldsymbol{\varepsilon}}^{vp} = \mu \left\langle \left(\frac{p'^d_c}{p'^r_c} \right)^N \right\rangle \frac{\partial f_d}{\partial \boldsymbol{\sigma'}} \tag{15}$$

200 where $\left(\frac{p'^d_c}{p'^r_c} \right)$ is the ratio the of intecepts of the two yield surfaces with the p' axis and N is a material parameter, or a

201 combination of material parameters. As it can be appreciated through eq. 15, the reference yield surface is associated to

202 a reference strain rate.

203 The size of the reference yield surface, and therefore the value of p'^r_c, only depends on the viscoplastic strains.

204 Accordingly, the evolution of p'^r_c is governed by the hardening rule of the reference hardening plasticity model , which

205 is usually given by an expression such as eq. (11).

206
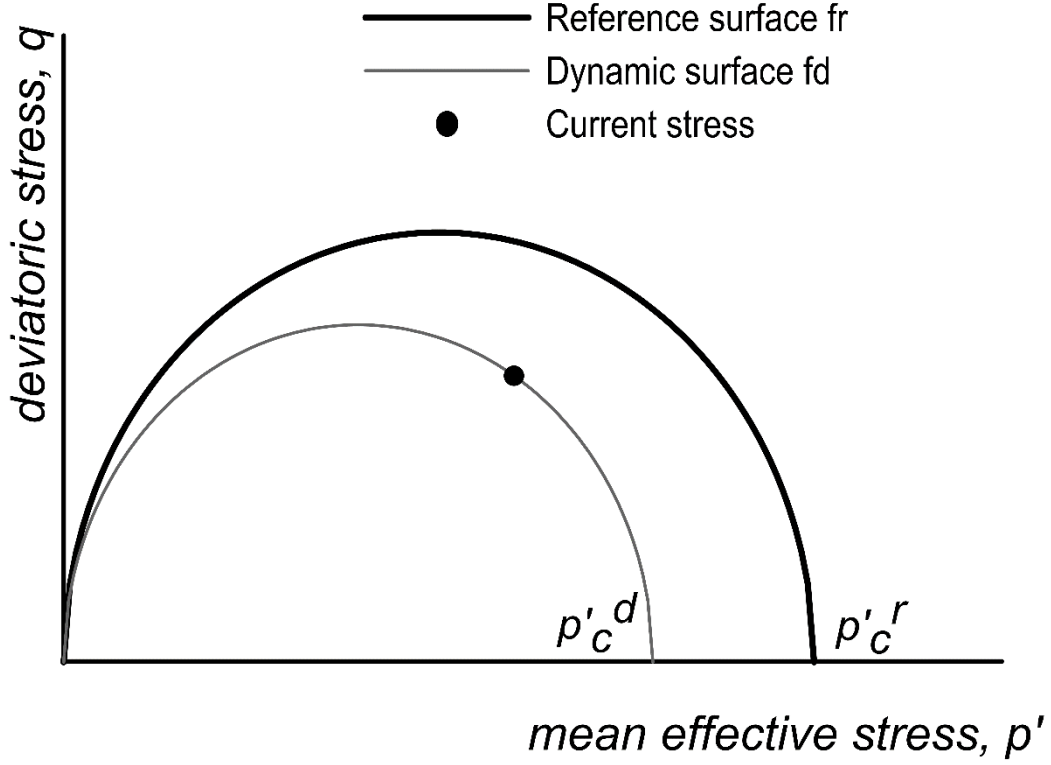
Fig. 2. Dynamic and reference surfaces. Depending on the current stress state, the dynamic surface can either be smaller or bigger than the reference surface.

2.3 Vermeer and Neher Model

'Creep models'are models of the Extended Overstress Theory built on experimental evidences gathered at constant effective stress (creep tests)[43]. The isotropic models described in Refs. 29 and 44 and the anisotropic model of Leoni et al.[47] are all 'creep models'. The formulation of the VNM[29] takes advantage of the results of standard oedometer tests, where the axial stress is increased stepwise and maintained constant for at least 24 hours. In such conditions, after pore pressure dissipation and consolidation, a creep phase takes place. When the applied stress is high enough, the viscoplastic strains grow linearly with the logarithm of time, and a creep index μ^* can be defined as:

$$\mu^* = \frac{\Delta \varepsilon_v^{vp}}{\Delta ln(t)} \tag{16}$$

where $\Delta \varepsilon_v^{vp}$ is the increase in the viscoplastic volume strain and t is time. By writing the viscoplastic volume strain at time $\tau = 24$ hours as $\bar{\varepsilon}_v^{vp}$, it follows:

10

$$222 \qquad \mu^* = \frac{\varepsilon_v^{vp} - \bar{\varepsilon}_v^{vp}}{\ln(t) - \ln(\tau)} \qquad (17)$$

223   so the relationship between time and viscoplastic strain is:

$$224 \qquad \frac{t}{\tau} = exp\left(\frac{\varepsilon_v^{vp} - \bar{\varepsilon}_v^{vp}}{\mu^*}\right) \qquad (18)$$

225   The viscoplastic volumetric strain rate is then:

$$226 \qquad \dot{\varepsilon}_v^{vp} = \frac{\mu^*}{\tau} exp\left(\frac{\varepsilon_v^{vp} - \bar{\varepsilon}_v^{vp}}{\mu^*}\right) \qquad (19)$$

227   In the VNM, the reference yield function f_r describes the state of the material which has been loaded for the reference

228   time τ. However, in light of eq. 18, it is also related to a constant strain rate $\dot{\varepsilon}_v^{vp} = \frac{\mu^*}{\tau}$.

229   The viscoplastic volume strains occurring during a creep phase induce hardening, *i.e.* the hardening parameter p'$_c^r$

230   evolves, with p'$_c^r$ = p'$_c^d$ when t = τ and p'$_c^r$ > p'$_c^d$ when t > τ. Adopting the hardening rule of the Modified Cam Clay:

$$231 \qquad \varepsilon_v^{vp} - \bar{\varepsilon}_v^{vp} = (\lambda^* - \kappa^*)\ln\left(\frac{p\prime_c^r}{p\prime_c^d}\right) \qquad (20)$$

232   with $\lambda^* = \frac{\lambda}{1+e}$ and $\kappa^* = \frac{\kappa}{1+e}$. By introducing eq (20) into eq. (19) the volumetric viscoplastic strain rate can be related to

233   the ratio between the dynamic and the reference surfaces:

$$234 \qquad \dot{\varepsilon}_v^{vp} = \frac{\mu^*}{\tau}\left(\frac{p\prime_c^d}{p\prime_c^r}\right)^{\frac{\lambda^* - \kappa^*}{\mu^*}} \qquad (21)$$

235   Consistency between eq.(15) and eq.(21) implies $N = \frac{\lambda^* - \kappa^*}{\mu^*}$ and $\mu = \frac{\mu^*}{\tau\frac{\partial f}{\partial p\prime}}$ and the substitution that follows into eq. (15)

236   provides the full viscoplastic strain rate tensor for the VNM.

237   Eq. (21) predicts that any loading process occurring at a certain constant strain rate is characterized by a fixed $\left(\frac{p\prime_c^d}{p\prime_c^r}\right)$ ratio.

238   Therefore Normal Compression Lines at different strain rates are expected to be parallel lines, and also the VNM is

239   consistent with the isotach concept. The reference yield function f_r describes then the combination of stress states for

240   which a Normal Consolidated type of behaviour applies whenever the load increments are imposed every 24 hours. The

241    $\left(\frac{p\prime_c^d}{p\prime_c^r}\right)$ ratio is a measure of the 'distance' from this state, and its inverse can be used to define an apparent Over

242   Consolidation Ratio (OCR). Differently from elasto-plastic models, the apparent OCR does not depend only on the

243 loading sequence and then on the maximum stress that had been applied. For instance, during a prolonged creep phase,

244 the OCR grows since $p'_c{}^d$ remains constant while $p'_c{}^r$ increases with the accumulated viscoplastic strains, in virtue of the

245 hardening rule (eq (11)).

246

247 **3. Experimental behaviour of clastic materials from the Adriatic basin and comparison with VNM**

248 **predictions**

249 A previous experimental characterization of the time-dependent behaviour of clastic materials from the Adriatic basin has

250 been described in Ref. 48. Sandy and clayey samples were loaded in the oedometer until reaching some stress higher than

251 the *in-situ* one, which was mantained constant for 2 weeks. Creep strains were appreciated, while when resumpting the

252 monotonic loading the compressibility of these samples was initially smaller than the one of analogous samples that had

253 not been exposed to creep. At higher stresses,the behaviour of the two types of samples was comparable again. Some

254 preliminary data suggested that the stress range over which the compressibility is reduced because of creep depends on

255 the OCR and on the duration of creep. The OCR also impacted on the creep rate. These evidences are similar to the ones

256 found for various soils or rocks (e.g. Refs. 35,36,49-53) and confirm that Adriatic sediments show appreciable viscoplastic

257 effects, such as those that might be taken into account by the VNM through the hardening law relating the yield stress to

258 the viscoplastic volume strains.

259 The present work, based on the results of a new comprehensive set of experimental tests, is aimed at:

260 - gaining a further insight on the mechanical behaviour of the Adriatic offshore sediments, accounting for different

261 loading histories and creep times;

262 - comparing the experimental findings with the results of simulations based on the VNM model;

263 - defining robust experimental protocols for the determination of the model parameters;

264 - providing the parameters for subsidence simulations for the fields of concern.

265

266 *3.1 Materials*

267 The experimental study was performed on clastic samples from the reservoirs of two fields (for confidentiality reasons

268 defined as Field 1 and Field 2 in the following), focusing on the evaluation of the viscoplastic behaviour. The grain size

269 distribution, obtained through laser diffractometry, and the related classifications are provided in Fig. 3 and Table 1.

270 While all the samples from the Field 1 reservoir were classified as silty sand and have about the same grain size

271 distribution, the samples from the Field 2 reservoir fall into two classes, one being a clayey silt and the other being a silty

272 sand.
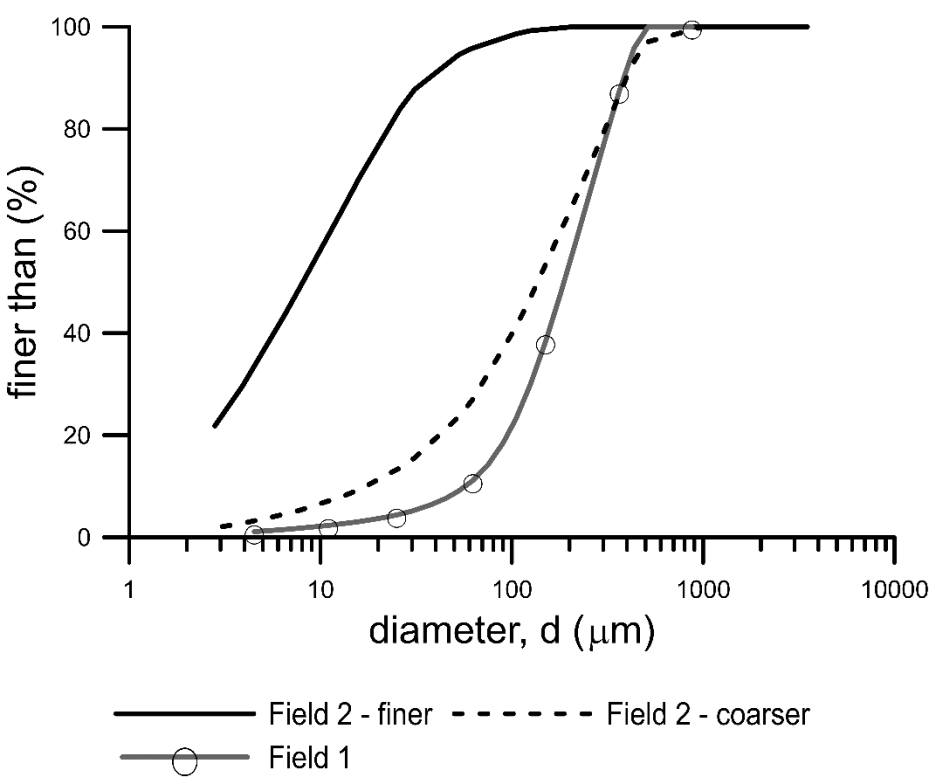
Fig. 3. Grain size distributions of studied samples

275 **Table 1**

276 Grain size fractions according to British standard 5930.

	Clay (d < 2 μm)	Silt (2 μm ≤ d < 60 μm)	Sand (60 μm ≤ d < 2 mm)
Field 1	1	10	89
Field 2 (finer)	22	74	4
Field 2 (coarser)	2	25	73

278 *3.2 Testing protocols*

279 Samples were water saturated and tested under oedometer conditions. For each material, three different multistage step

280 Loading Sequences (LS) were adopted (Fig. 4):

13

281 LS 1: the axial stress σ_a was increased every 24 hours as in 'conventional' oedometric tests. No prolonged creep phases

282 were imposed. A comparison of the results of this procedure with other sequences was made, to verify the possibility of

283 determining the parameters of the VNM with relatively quick, standard procedures;

284 LS 2: the axial stress σ_a was increased every 24 hours up to a value higher than the geostastic one (equal to 10.2 MPa for

285 Field 1 and 9.3 MPa for Field 2). σ_a was then kept constant for two weeks to induce a well developed secondary

286 compression. The stress increments which followed were applied in small steps to appreciate possible hardening due to

287 creep, detected as an increase of the apparent preconsolidation stress;

288 LS 3: the axial stress was first increased every 24 hours up to $\sigma_a = 8$ MPa, a stress which is smaller than the geostratic

289 one for all samples, where a first creep phase of two weeks was imposed. They were then further loaded up to 16 MPa

290 with increments of 2 MPa imparted every 24 hours, and unloaded back to 8 MPa with the same progression. The axial

291 stress was then increased to $\sigma_a = 10$ MPa and a second creep phase of two weeks was imposed. A final loading – unloading

292 cycle up to 58 MPa applying the load increments every 24 hours was then imposed. This loading sequence was aimed at

293 checking the relevance of creep from Over Consolidated states. Since the loading history is an important information for

294 proper modelling with the VNM, the loading – unloading sequence imposed before the creep stage at $\sigma_a = 10$ MPa was

295 chosen to make at least the recent history available for modelling.

296

14
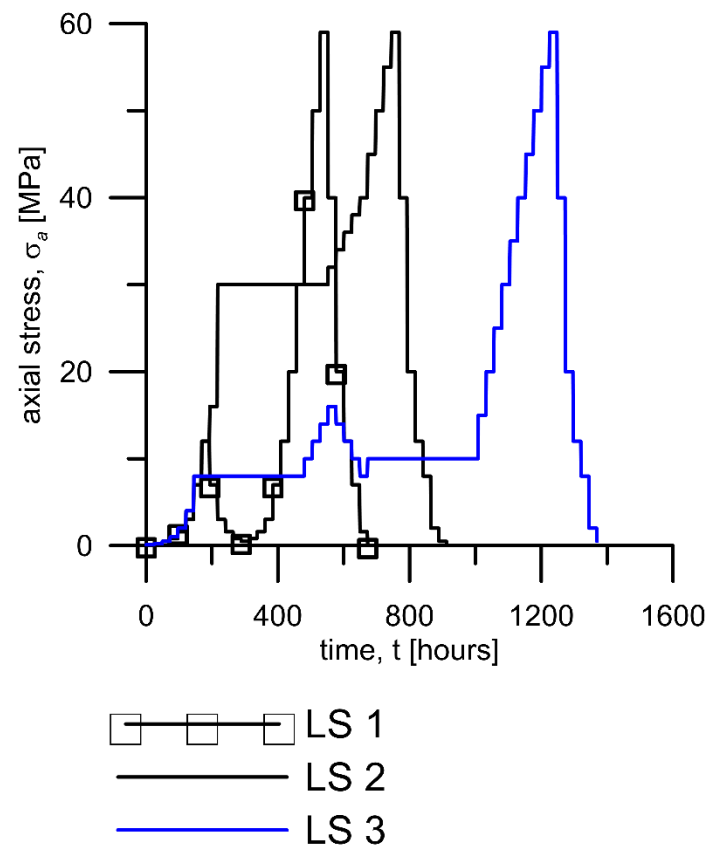
297 **Fig. 4.** Loading sequence adopted in the multistage oedometer loading tests

298 Constant strain rate triaxial with null lateral strain tests (CRS-K$_0$) previously performed on dry Field 1 samples[54] were

299 also reinterpreted. In these tests, the axial stress was first increased at a constant strain rate up to $\sigma_a = 15$ MPa, and it was

300 then kept constant while recording the creep strains. Subsequently, loading and unloading were applied by imposing again

301 constant strain rates.

302 *3.3 Experimental results and model predictions*

303 This section presents the results of laboratory tests together with the predictions of the numerical modelling performed

304 using the VNM model. The same type of mechanical response was obtained with all the materials and the discussion is

305 here limited to the Field 2 samples. In the simulations the specimens were treated as a reference elementary volume, eq.

306 (15) was discretized in time and solved numerically with the software Matlab®. The numerical implementation was done

307 accounting for the constraints of null radial and circumferential strains which hold in oedometer conditions. In the LS

308 tests the axial stress was increased by steps and the saturated samples also experienced mechanical consolidation, which

309 according to the interpretation in the frame of the Terzaghi's one-dimensional equation occured within 10 minutes from

310 each load increase. Consistently, the experimental creep strains, labeled as ε_a^* in the following, are determined as the

311 difference between the current axial strain ε_a and the axial strain at the end of consolidation, *i.e.* 10 minutes after imposing

312 the load. In the numerical analyses the consolidation process was approximated by adopting load ramps of 10 minutes.

313 Fig. 5a shows the experimental stress-strain curve and the model predictions for the LS1 test. The figure provides the

314 axial strain ε_a at the end of the consolidation and 24 hours from loading for each step. The model reproduces quite well

315 the experimental results, in particular for stresses higher than about 12 MPa and along the unloading – reloading sequence.

316 Fig. 5b provides the time history of the creep strains ε^*_a for selected stresses. ε_a^* increases about linearly with the logarithm

317 of time, with a rate that at first increases with the stress and becomes about constant for $\sigma'_a \geq 30$ MPa. The slope of ε_a^*

318 vs. ln(t) at high stresses was used to evaluate the μ^* parameter of the VNM, while the slopes of the loading and of the

319 unloading – reloading lines, defined for the 24 hours strains $\bar{\varepsilon}_a$, were used to determine λ^* and κ^*, respectively. The

320 dependency of the experimental strain rate on the stress is in agreement with the predictions of the VNM model. According

321 to eq. (21), the strain rate grows with the p'^d_c/p'^r_c ratio. At lower stresses the specimen is overconsolidated and this ratio

322 is surely smaller than one, which justifies small strain rates. At high stresses the $\left(\dfrac{p'^d_c}{p'^r_c}\right)$ ratio at 24 hours is equal to one

323 which justifies identical strain rates for each step.

324

15
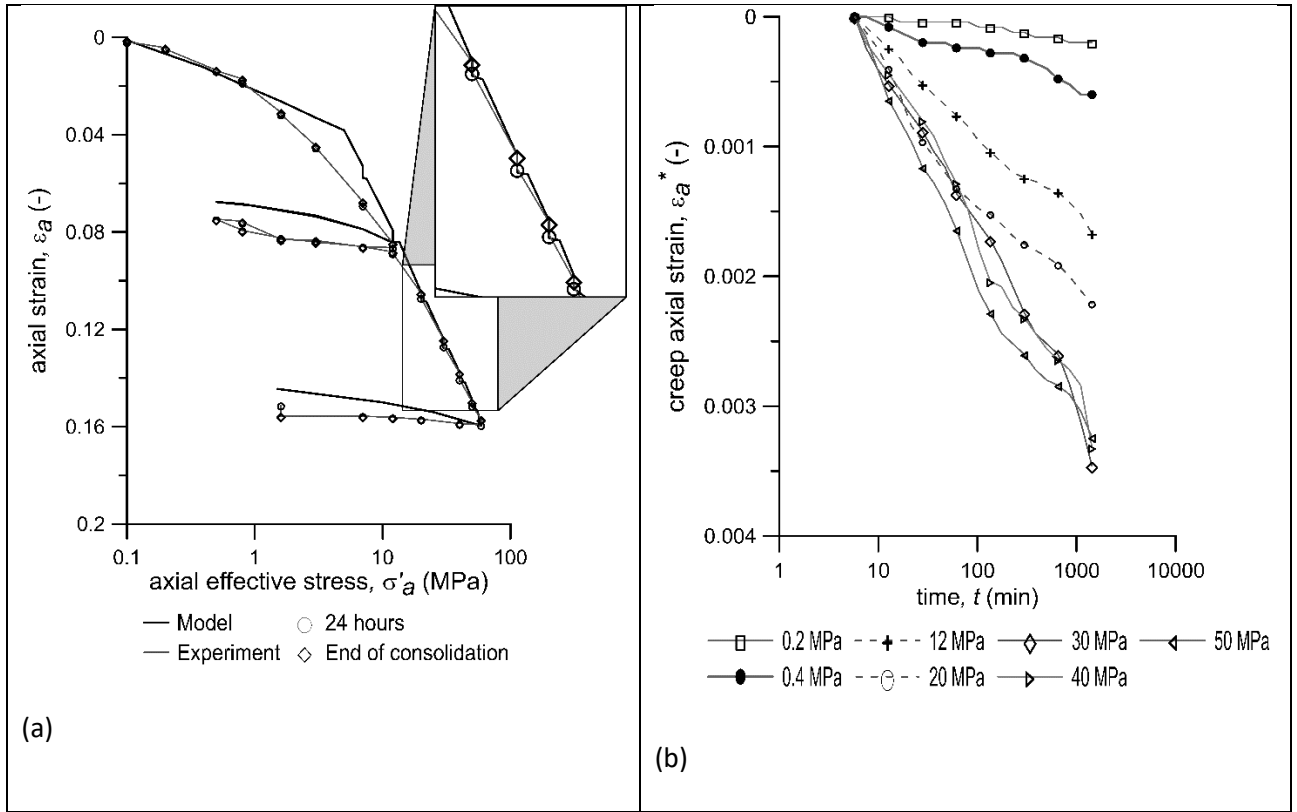
Fig. 5. LS1 test on coarse Field 2 sample. a) stress – strain curves. b) creep strains vs. time

The impact of 14 days of creep, such as the one occurring when $\sigma_a = 30$ MPa in the LS2 tests, is shown in Fig. 6. Besides causing larger axial strains, the long creep phase impacts on the behaviour in two ways, which become clear when the axial stress is furtherly increased. For one, the material is stiffer than before. For another, the creep strains accumulating during 24 hours in the following load steps are reduced with respect to the ones occurring at the stresses which preceed the long creep stage. In Fig. 6, the 24 hours creep strains are appreciated as the vertical distance between empty and grey circles. The dashed line provides the position of the Normal Compression Line under oedometer conditions for the 24 hours strain, which gives the relationship between the axial stress on the reference surface and ε_a. After the 14 days creep, the state of the specimen plots to the left of the NCL, justifying an apparent overconsolidation effect and the stiffer behaviour. However, under very high stresses ($\sigma'_a \geq 45$ MPa) the experimental points align again very well with the NCL and the creep strains attained during 24 hours are comparable with the initial ones.
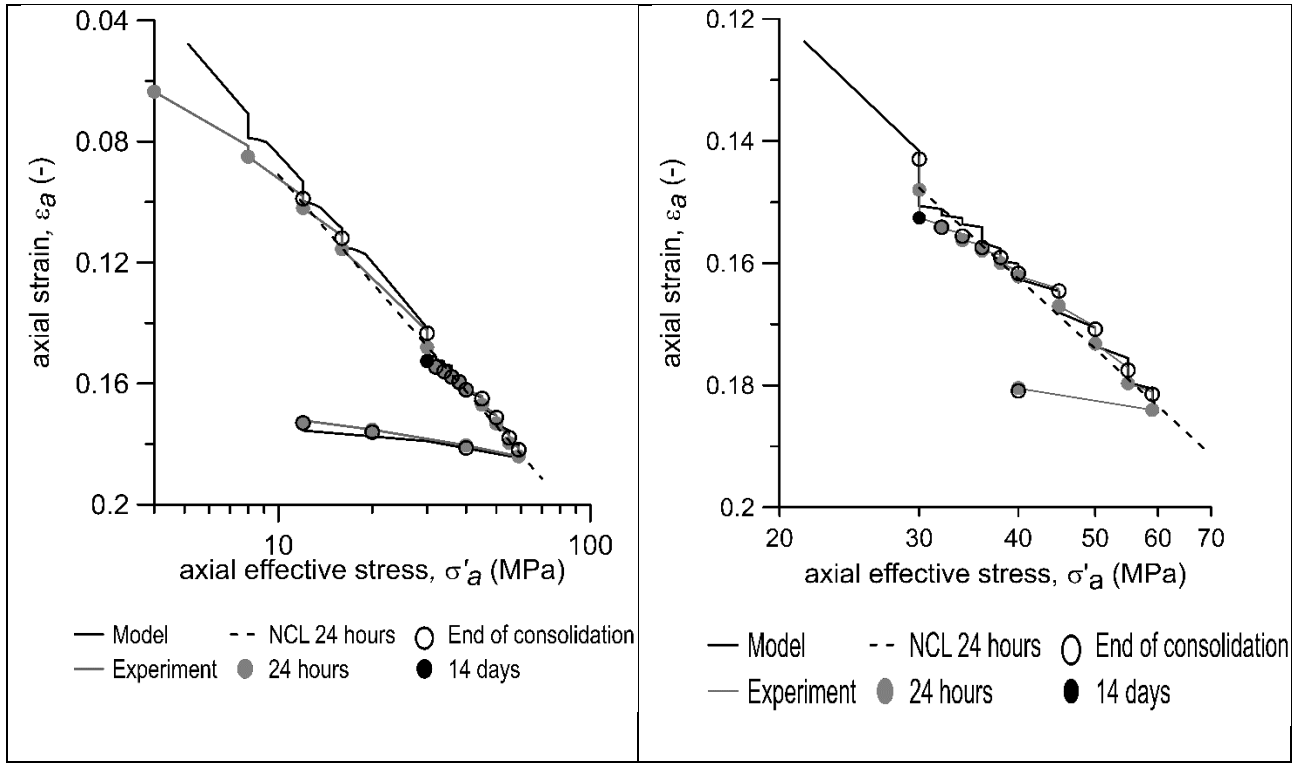
Fig. 6. LS2 test on coarse Field 2 sample. a) stress – strain curve, b) zoom on the hardening due to 14 days of creep

This effect can be further appreciated by observing the time history of the creep strains under different loads in Fig. 7a. $\sigma'_a = 16$ MPa and $\sigma'_a = 30$ MPa were both applied starting from a physical state which plots on the oedometer NCL, *i.e.* with $\frac{p'^d_c}{p'^r_c} = 1$ and consistently with eq (21) the strain rate developing under these loads is the same. However, because of the large strains accumulating during the 14 days of creep, the loads ranging from $\sigma'_a = 32$ MPa to 38 MPa are imparted from physical states on the left of the NCL, i.e. with $\frac{p'^d_c}{p'^r_c} < 1$. When these loads are applied the sample has then developed some apparent OCR, which, in light of eq. (21), justifies smaller strain rates. At higher stresses the experimental points plot on the NCL and the previous strain rate is obtained again when $\sigma'_a = 55$ MPa. Fig. 7b examines the effects on the creep strains of a loading - unloading – reloading sequence (LS3 test). Following a reloading step, such as under the $\sigma'_a = 10$ MPa imposed for 14 days in LS3, the creep strain rate is highly reduced. However, as a first loading condition is approached, the strain rates increases ($\sigma'_a = 16$ MPa) and it gets to a quite constant value at higher tress ($\sigma'_a = 25$ MPa and $\sigma'_a = 40$ MPa). It is interesting to note that the strain rate does not depend on the duration of the current creep phase, as in Fig. 7a the strain rates for 16 MPa, 30 MPa and 55 MPa are all the same, so that it can be concluded that a creep phase of 24 hours should be enough for a reliable characterization, provided that it is imparted from a condition such that $\frac{p'^d_c}{p'^r_c} = 1$.
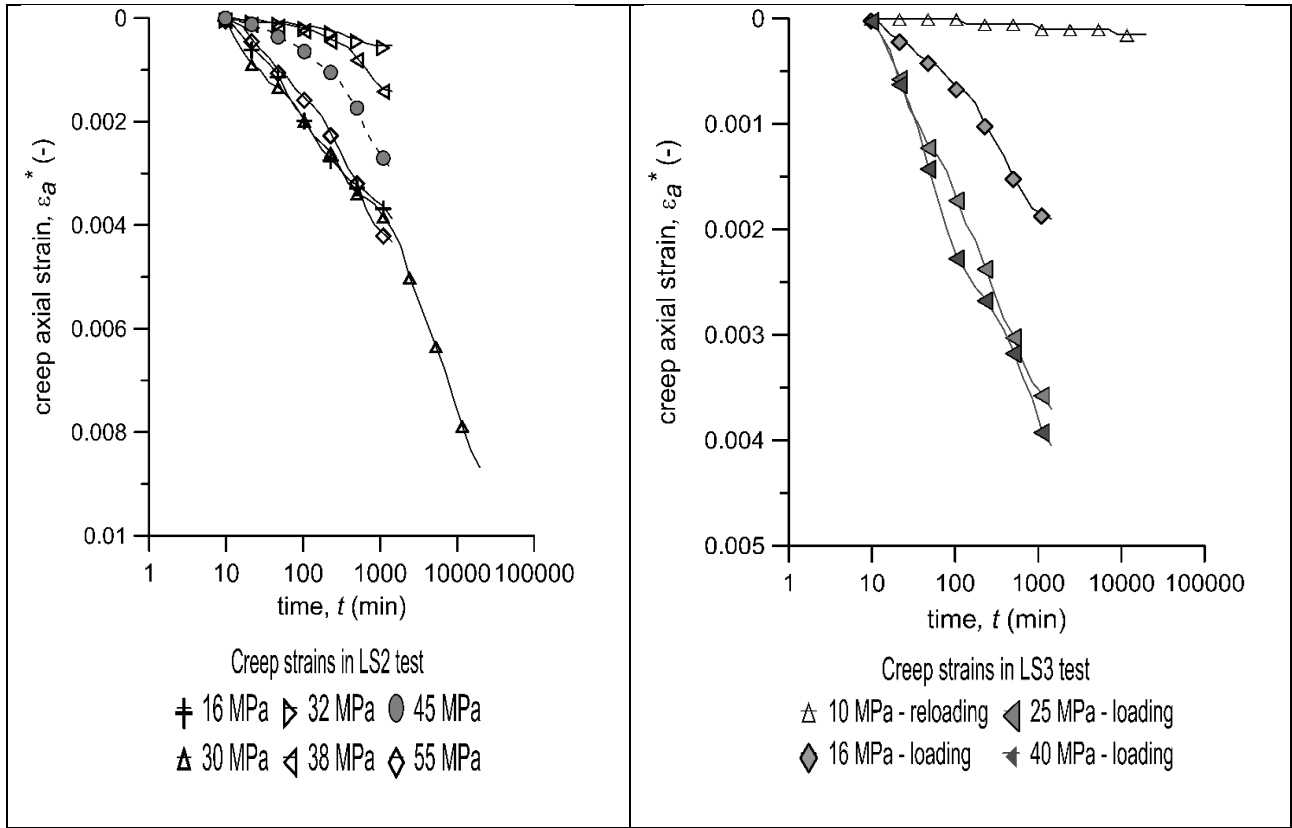
Fig. 7. Effect of history on strain rates. a) creep strains from a monotonous loading sequence, with a long creep at σ'$_a$ = 30 MPa (LS2); b) creep strains from a loading – unloading – reloading sequence (LS3).

Model capabilities were also checked against conditions of imposed strain rate. Fig. 8 shows the strain history (a) and the stress – strain relationship (b) for one of the CRS-K$_0$ tests on a Field 1 sample. The hardening effect of creep is well evident both in the experiment and in the simulations, which prove to be adequate also for the different material and testing conditions.
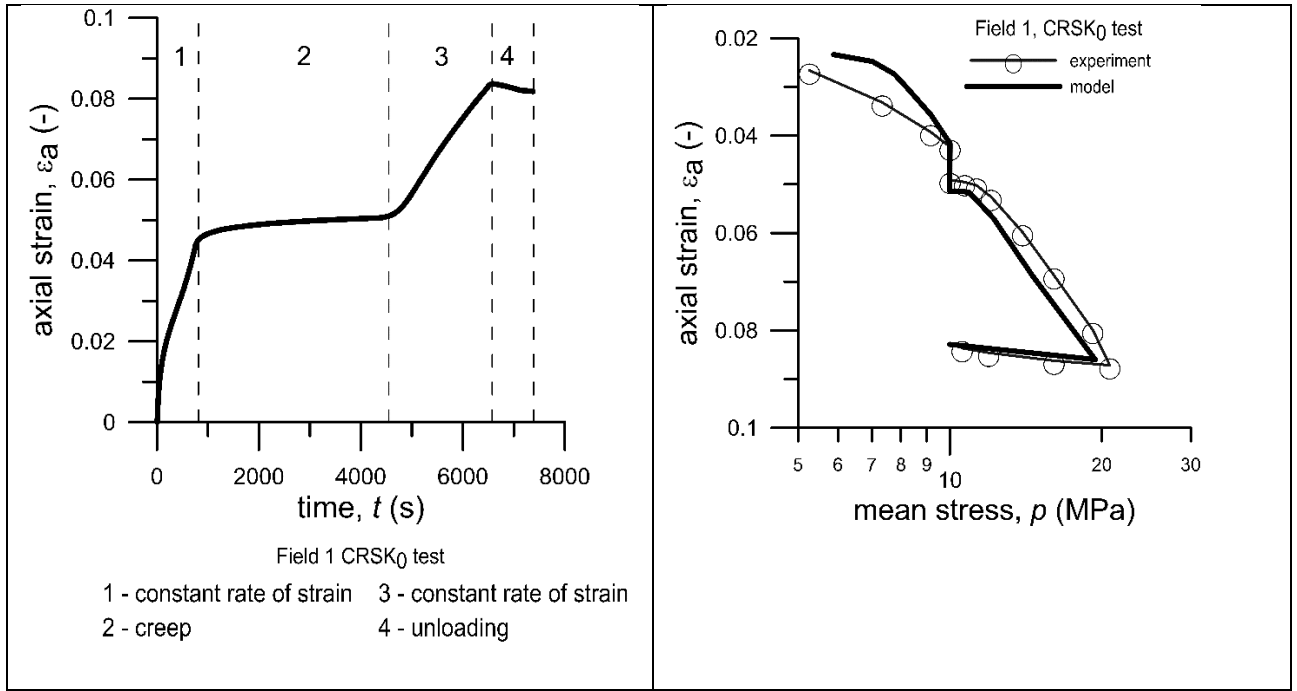
Fig. 8. CRS-K_0 test on Field 1 sample. (a): strain history. (b): stress - strain curve.

Table 2 provides the ranges of parameter values estimated from each test, which were also used in their simulations. As for the Field 1 case, no significant influence of testing procedure on parameters was found.

Table 2

Range of parameter values determined from the laboratory tests.

	λ^* (-)	κ^* (-)	μ^* (-)
Field 1 – step load oedometer	$6.1 \div 6.8 \ 10^{-2}$	$0.5 \ 10^{-2}$	$1.5 \div 1.7 \ 10^{-3}$
Field 1 – CRS-K_0	$5.0 \div 6.8 \ 10^{-2}$	$0.7 \div 1.1 \ 10^{-2}$	$1.1 \div 1.5 \ 10^{-3}$
Field 2 – coarse	$4.8 \div 7.6 \ 10^{-2}$	$0.2 \div 0.8 \ 10^{-2}$	$0.5 \div 1.3 \ 10^{-3}$
Field 2 – fine	$6.8 \div 7.0 \ 10^{-2}$	$1.1 \div 1.2 \ 10^{-2}$	$1.4 \div 1.8 \ 10^{-3}$

4. Case Histories

The experimental campaign and related numerical simulations suggested that the VNM can provide a quite good reproduction of the behaviour in oedometer conditions of reservoir samples from two gas fields. This section presents the results of the studies of the real field cases for the two fields, carried out through Finite Element simulations and adopting the VNM as described in section 2.3. As stated, the two fields are located in the northern and central portions of the

19

372 Adriatic Sea. In this area, gas reservoirs are generally constituted by alternances of sandy and shaly layers, deposited

373 during the Pliocene and Pleistocene ages (Carola formation till Porto Garibaldi formation) that form multilayered systems

374 in which every layer may have its own gas-water contact and a thickness variable from a metric scale to thin layers of

375 few centimeters. The shaly layers are the source rocks of the biogenic gas while the trapping mechanism can be

376 structural/mixed structural or stratigraphic type. Porosity of hydrocarbon bearing sandy layers is very variable, from very

377 low values in thin beds environments up to more than 25% in conventional reservoirs. Gas from Adriatic Sea fields is

378 generally withdrawn through several wells whose production is gathered toward one or more platforms per field. Most of

379 these platforms are equipped with a continuous GPS station for the monitoring of subsidence evolution. In several fields,

380 a well is equipped with radioactive markers for the measurements of the compaction of the reservoir rock in time[6,55,56].

381 The companies operating the gas fields are in charge of providing, and periodically updating, subsidence forecasts for

382 each field based on detailed 3D numerical fluid-dynamic and mechanical models in order to demonstrate the

383 environmental sustainability of their activities. The results of these models have to correctly reproduce the historical

384 monitoring data acquired in the field: the two real cases presented in this section aim at highlighting the improvement in

385 the accuracy of these studies achieved through the adoption of the VNM model, whose implementation in a FE code was

386 previously tested against synthetic cases[57-58].

387 Herein, all subsidence values for each field were normalized with respect to the maximum subsidence obtained in the

388 simulation performed with the VNM constitutive model at the GPS station location.

389 *4.1 Workflow*

390 First, a 3D geological model was built starting from reflection seismics and populated with petrophysical properties from

391 well logs and laboratory analysis of core samples. Next, the geological model was converted into a Finite Difference

392 fluid-dynamic model of the reservoir, that evaluates the time evolution of pore pressures in the whole computational

393 domain. Pore pressure fields at selected time steps were finally provided, in a one-way coupled framework, to the 3D

394 finite element geomechanical model, built using the commercial software Abaqus®.

395 To correctly evaluate the evolution of the stress state above and around the reservoir and, consequently, correctly predict

396 the evolution of land subsidence, the geomechanical model also includes the rocks surrounding the reservoir, namely the

397 overburden, underburden and sideburden regions. The reservoir rocks were described by means of appropriate elasto-

398 plastic or elasto-viscoplastic constitutive laws (e.g. Modified Cam-Clay - MCCM - and VNM for the present cases,

399 whose parameters were derived from the laboratory tests described in section 3), while the rocks surrounding the reservoir

400 were considered as linear elastic. Appropriate stress-dependent rock compressibilities were used in the fluid-dynamic

401 model to ensure consistency with the mechanical behaviour in the geomechanical model. Because of the non linear,

402 anelastic behaviour of the reservoir rock, the geomechanical predictions depend on the initial stress state, which must be

403 identified adequately (see e.g. Refs. 59-60). Here it was determined as follows: the total vertical stress was obtained by

404 integrating the bulk density profile versus depth, while the horizontal stress was obtained combining drilling information,

405 stress tests and regional data when available. Boundary conditions imposed to the model prescribe null horizontal

406 displacements of the lateral faces and no displacement in the three directions at the bottom face. Initial geostatic

407 equilibrium is achieved by imposing the gravity force at the model elements. The simulations were then carried out

408 allowing the model to evolve, following the time variation of pore pressure values derived from the fluid-dynamic

409 simulation at each time step. Simulations were continued for 30 years after the end of production, in order to evaluate the

410 effect of pore pressure equilibration after shut down.

411 While for elasto-plastic models like the MCCM, the initial position of the yield surface, determined by the parameter p'_c

412 in eq. (2), only depends on the maximum stress ever experienced by the material, in the case of elasto-viscoplastic models

413 like the VNM, the definition of the initial position of the reference yield surface, *i.e.* of $p'_c{}^r$, requires a more elaborated

414 approach that also takes into consideration time and strain rates. In fact, the initial viscoplastic strain rate of the model

415 must be consistent with the one of the material *in situ*, which in light of eq. (21) provides a constraint on the initial value

416 of the $\left(\frac{p'_c{}^d}{p'_c{}^r}\right)$ ratio. For the Adriatic basin it is reasonable to assume a constant strain rate induced by the sedimentation

417 process, given by:

$$\dot{\varepsilon}_v^{sed} = -\frac{\Delta e}{(1+e_0)\Delta t} \tag{22}$$

419 where e_0 is the void ratio at the beginning of sedimentation and Δt is the age of the sediments. The viscoplastic component

420 of the sedimentation strain rate was obtained by subtracting the elastic component from the total one, i.e. as $\frac{\lambda^*-\kappa^*}{\lambda^*}\dot{\varepsilon}_v^{sed}$

421 The initial value of the apparent OCR, *i.e.* the $\left(\frac{p'_c{}^r}{p'_c{}^d}\right)$ ratio, can then be obtained by inverting eq. (21):

$$\text{OCR} = \left(\frac{\lambda^*-\kappa^*}{\lambda^*}\frac{\tau}{\mu^*}\dot{\varepsilon}_v^{sed}\right)^{-\frac{\mu^*}{\lambda^*-\kappa^*}} \tag{23}$$

423 *4.2 Field 1*

424 Field-1 is an off-shore gas field located in the Adriatic Sea at about 20 km from the Italian coastline, with an average

425 water depth of about 20 m. The reservoir is included in the Lower Pliocene sequences, situated from 1000 to 2200 mssl,

426 characterized by an alternation of metric and plurimetric sandy, clayey and silty layers with variable proportions and

427 thicknesses, classified as a proximal turbidite deposit in submarine fan facies. The field is bounded by a lateral facies

428 variation toward north and east and by a NW-SE fault in the south west direction. Fourteen wells have been drilled in the

field and connected to the same production platform. A GPS station, located on the platform, was installed about 10 years
after the start of production and has been recording data for more than 11 years.

The FE geomechanical grid of Field 1 consists of about 300,000 cells, resulting in more than one million degrees of
freedom. Subsidence induced by production was simulated with alternative constitutive laws for reservoir rocks, *i.e.*
elasto-plastic (MCCM) and elasto-viscoplastic (VNM). The simulation results were then compared to the vertical
displacements recorded by the GPS station. As a first attempt, the λ and κ parameters for the MCCM introduced in the
simulations were imposed as the mean values determined with all the laboratory tests on Field 1 samples (Table 2). For
the eleven years of GPS recording, the MCCM predictions obtained following this approach ("MCCM_lab" in Fig. 9),
are far from the GPS data. A further simulation was then performed with MCCM constitutive law, tuning λ and κ
parameters (assuming different values in each geological layer) in order to better reproduce the GPS data: in this case the
simulated evolution of subsidence ("MCCM" curve in Fig. 9) is much closer to the GPS series, but the subsidence trend
is not correctly reproduced. The simulated curves show a slope change after about 7 years from the start of GPS recording
(year 10 in the figure), which is not present in the GPS data. In both the MCCM models, the subsidence velocity increases
because of a fast pressure drop due to a sharp increase in production rates, which however did not impact immediately on
the recorded subsidence. This suggests that an elasto-plastic model may not be appropriate to describe the behaviour of
the reservoir rocks, since it instantaneously responds to pressure changes, while the role of a viscous component cannot
be neglected. The elasto-viscoplastic characterization of the reservoir rock enabled to better capture the subsidence history
recorded by the GPS ("VNM" curve in Fig. 9). The VNM simulations were carried out using the mean values of λ^* and
κ^* from the laboratory tests (Table 3), analogously to the first MCCM case, while only the creep index μ^* was calibrated
within the admissible range from the experiments. The initial value of the apparent OCR was computed through the
procedure described in section 4.1 and subsequently tuned on the basis of GPS data: the age of sediments was assumed
equal to 3.8 millions of years according to previous sedimentological studies, the average value of the intercept of the
NCL line determined from all oedometric tests (0.74) has been considered representative of the void ratio at the beginning
of sedimentation and the current void ratio has been set equal to 0.3 according to current in situ porosity. Fig. 10 shows
the modelled evolution of subsidence for the three cases, during the whole time-span from the start of production to the
end of the simulation.

Table 3

Adopted mechanical parameters for "MCCM_lab" and calibrated "VNM" simulations of Field 1. All parameters are
dimensionless.

22

|		
λ	elasto-plastic compliance ("MCCM_lab" case)	$7.96 \cdot 10^{-2}$
κ	elastic compliance ("MCCM_lab" case)	$8.61 \cdot 10^{-3}$
κ*	elastic compliance (strain)	$6.63 \cdot 10^{-3}$
ν	Poisson's ratio	0.3
λ*	elasto-viscoplastic compliance	$6.13 \cdot 10^{-2}$
M	CSL slope	1.33
μ*	creep index	$1.30 \cdot 10^{-3}$
OCR	apparent Over Consolidation Ratio	1.53

458
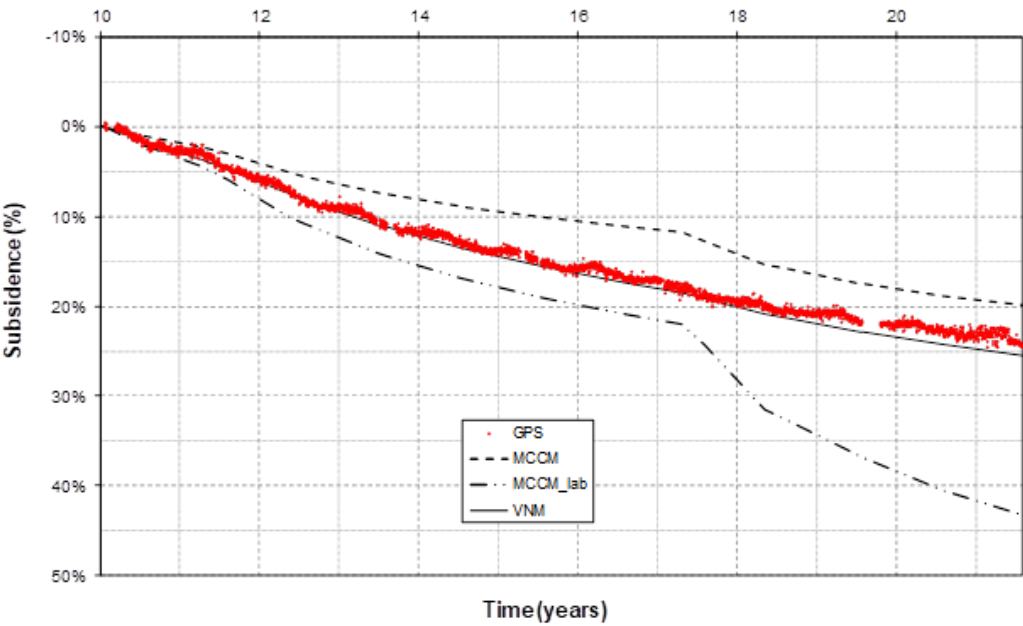
459

460 **Fig. 9.** Field 1: Comparison between evolution of measured and modelled vertical displacements from start of GPS recording

461

23
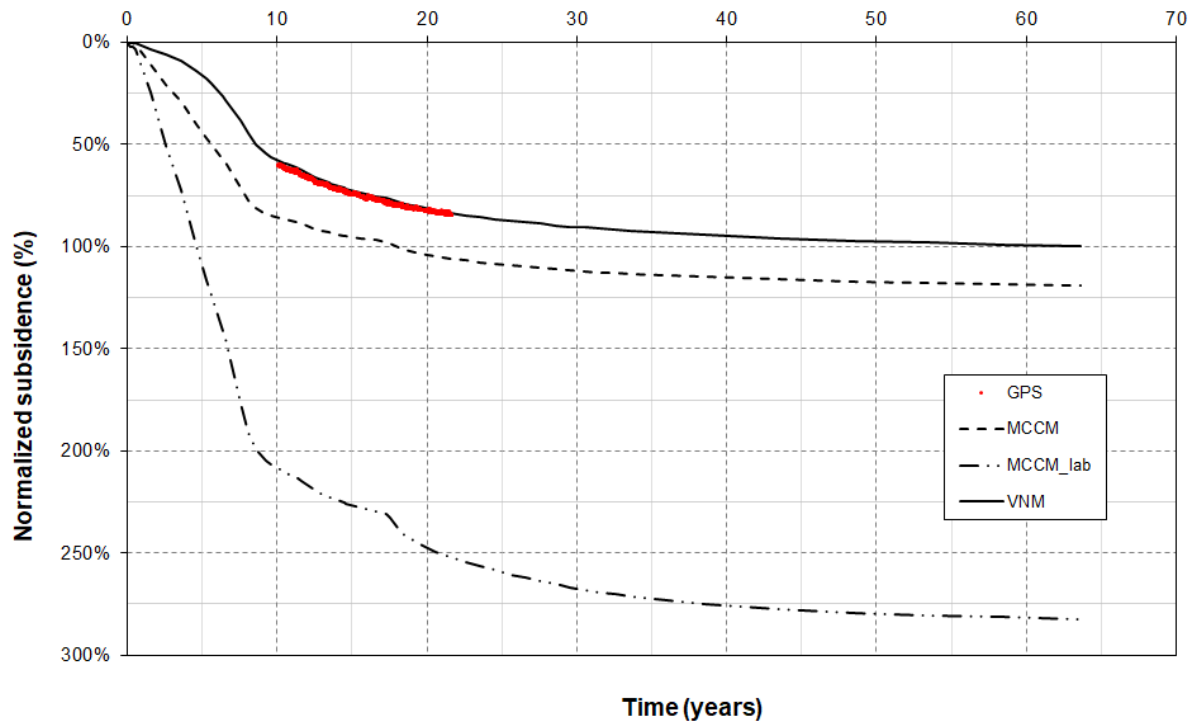
Fig. 10. Field 1: Evolution of modelled vertical displacement from the start of production to the end of the simulation, with comparison with GPS series.

A bathymetric survey was carried out around 10 years after the start of production, *i.e.* approximately at the same time when the platform was equipped with the GPS station. This survey allowed to build a map of the subsidence bowl, as the difference between the assumed undisturbed sea bottom regional trend and the bathymetry measured by the survey. The resulting map is shown in Fig. 11, together with the position of two sections of interest. In Fig. 11, the iso-subsidence lines predicted with the VNM are overimposed to the measured ones.

472
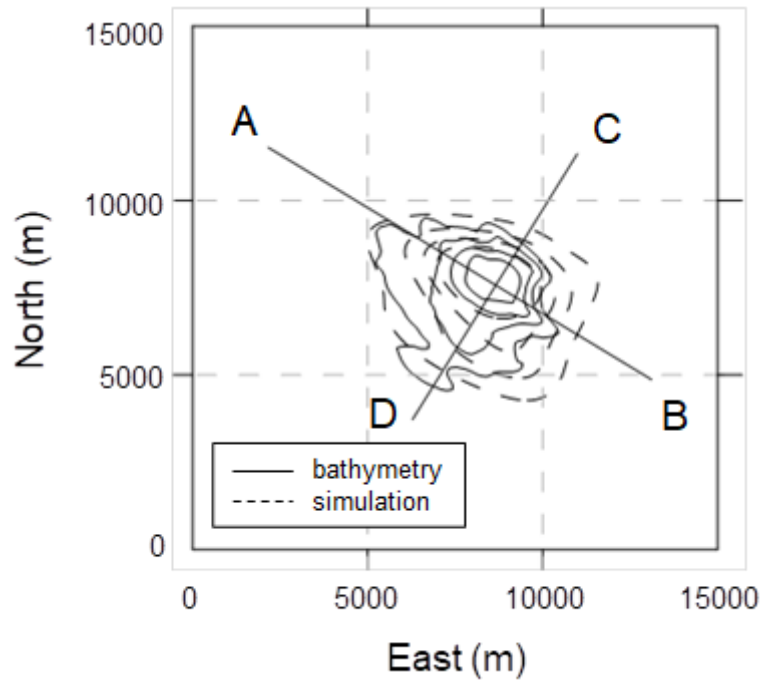
473 **Fig. 11.** Field 1: Subsidence from bathymetric survey and from model (contour lines 10%, 20%, 30%, 40%) and position of AB and
474 CD sections.

475

476 A comparison between the results of the geomechanical studies and the subsidence after the first 10 years of production,

477 as obtained from the bathymetric survey along the sections highligthed in Fig. 11, is shown in Fig. 12. Despite the fact

478 that, for the following 11 years of GPS monitoring, subsidence is overestimated by the MCCM_lab simulation and it is

479 slightly underestimated by the MCCM with GPS calibrated parameters (Fig. 9), at the time of the bathymetry the two

480 elasto-plastic simulations are coherent in overestimating both the depth and extent of the subsidence bowl. Remarkably,

481 the VNM simulation is able to accurately reproduce both the depth and the extent of the subsidence bowl directly using

482 the laboratory derived parameters.

483

484
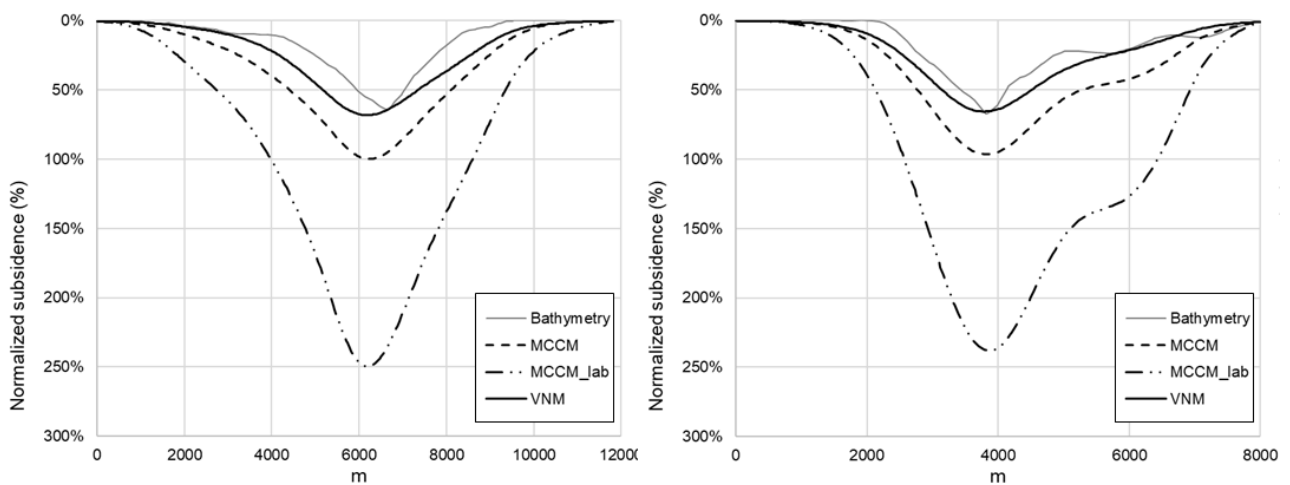
    Fig. 12. Field 1: Subsidence from bathymetric survey and modelled subsidence along sections AB (a) and CD (b).

486

487   *4.3 Field 2*

488 This off-shore gas field is located in the Adriatic Sea, at about 60 km from the Italian coastline, where the average water

489 depth is around 60 m. Its structure is made up by an anticline with two culminations. The proximal turbiditic sand lobes

490 of the pleistocenic Carola Formation represent the shallowest and most recent reservoir layers, while the deepest reservoir

491 layers (pliocenic Porto Garibaldi Formation) are composed by distal turbidite sand lobes and fringes. These sandy

492 reservoir layers lie from 900 to 1800 mssl and gas is withdrawn by 28 wells, connected to platforms A and B. The two

493 platforms are equipped with GPS stations that have been acquiring data since the early production phases. GPS records

494 highlight a delay between gas production rate and vertical displacement rate variations, as shown in Fig. 13 for platform

495 B. One well of platform B has been equipped with markers for the monitoring of reservoir compaction and bathymetric

496 surveys have been performed before the start of production of Field 2 and after 7 years.

497 The simulation domain was extended to the North-East of Field 2 to include two nearby gas reservoirs that are potentially

498 interacting hydraulically and mechanically, thus resulting in an extent of the model of about 88 km x 73 km x 5 km. The

499 model was discretized with about $5.5 \cdot 10^5$ finite elements, for a total of around $2 \cdot 10^6$ degrees of freedom.

500 Initial simulations were performed with VNM material properties from average experimental values (tests described in

501 section 3), while the initial value of the apparent OCR was defined according to the procedure proposed in section 4.1

502 and by adopting the same hypoteses described for Field 1 case (age of sediments equal to 1.4 millions of years, void ratio

503 at the beginning of sedimentation equal to 0.63 and current void ratio equal to 0.28). Then, a tuning of the VNM

504 parameters allowed to accurately reproduce the GPS data recorded at platform B (Fig. 14). This step involved only minor

505 changes of the creep index μ^* (less than 4%) and of the apparent OCR (around 1%), while λ^* and κ^* were left unchanged

506 (see Table 4).

507 In Fig. 15 the results of the simulation performed with the VNM are compared to those obtained using the MCCM whose

508 parameters (λ and κ) are derived from laboratory experiments according to the well known expressions in section 2.3 and

509 reported in Table 4. The OCR of the MCCM simulation was set equal to the ratio between the maximum vertical stress

510 reasonably compatible with the tectonical and sedimentological history of the area and the current stress (OCR = 1.20) as

511 higher values would not be justifiable. This comparison highlights that VNM is able to provide an excellent match of

512 monitoring data by directly using laboratory derived parameters and reasonable assumption on the consolidation state of

513 the material.

514 While GPS data from platform B were used to tune the VNM parameters, other available data (markers, bathymetry and

515 GPS on platform A) were used to validate the geomechanical model. To this purpose, Fig.s 16 and 17 show comparisons

516   of model results in terms of reservoir compaction from markers and iso-subsidence lines from bathymetries, respectively.

517   In particular, Fig. 16 shows the good agreement between cumulative compaction observed at the monitoring well and the

518   VNM model estimates. All the measurements are reproduced within the confidence interval (+/- 3 standard deviation) or

519   slightly overestimated, except for the measure acquired at year 11.7, which is out of trend and might be affected by

520   acquisition uncertainties. The subsidence developed in the 7 years between the two bathymetric surveys is well reproduced

521   by the model results (Fig. 17). Even if calibrated on data from platform B, the model properly reproduces also the

522   subsidence rate recorded at the GPS station installed on platform A (Fig. 18).

523   Finally, Fig. 19 shows the time evolution of the 2 cm iso-subsidence line, the minimum distance from the coastline and

524   the maximum extent at simulation-end, which is set 30 years after the production-end. It is apparent that the extent of the

525   subsidence bowl after end of production tends to stabilize with time, expecially in the direction of the coastline.

526

527

528
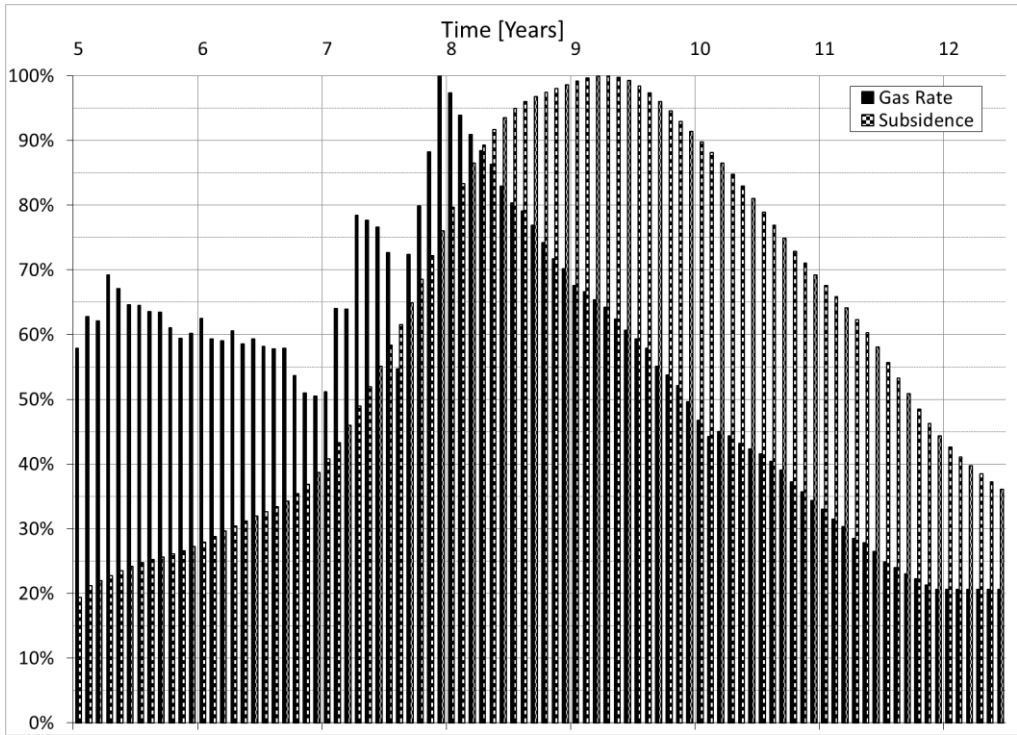
530   **Fig. 13.** Monthly data for platform B: gas production rate (black bars) versus subsidence GPS rate filtered from

531   seasonal components (black and white bars).

532
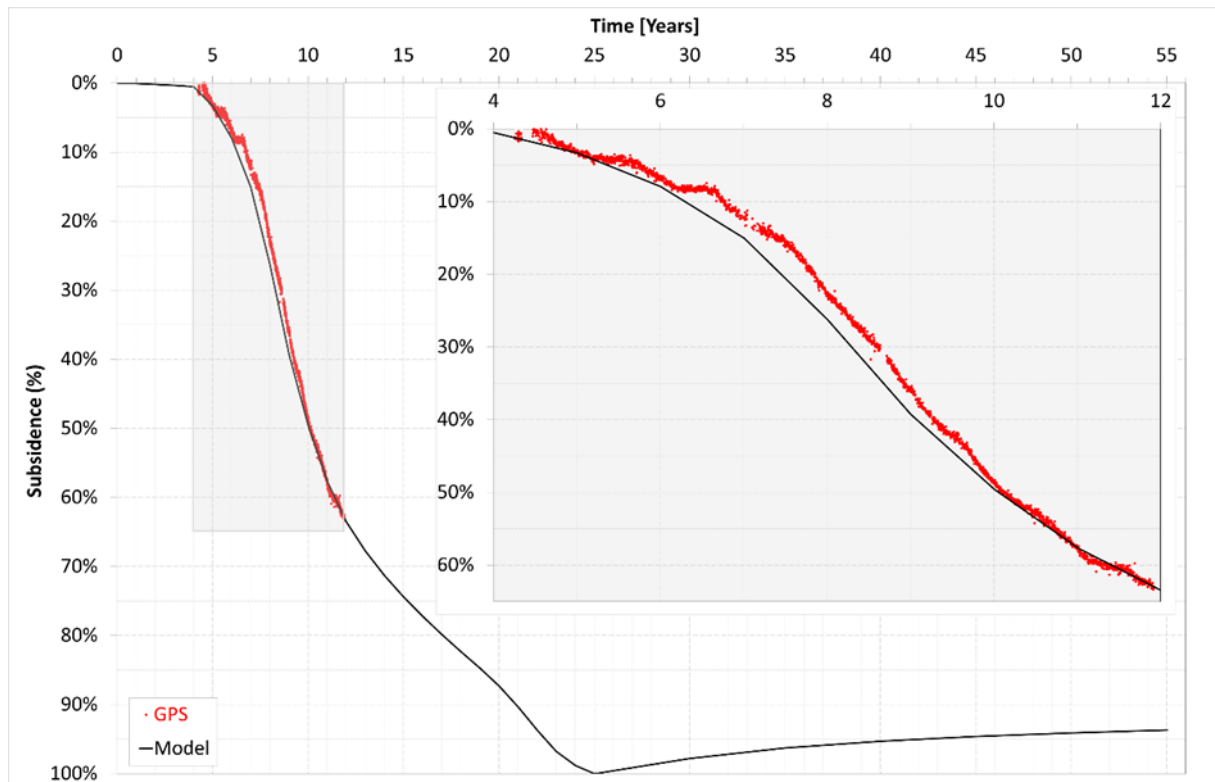
Fig. 14. Time evolution of subsidence at platform B (Field 2): GPS data versus model estimate, with magnification.

Table 4

Adopted mechanical parameters for "MCCM" and calibrated "VNM" simulations of Field 2. All parameters are dimensionless.

λ	elasto-plastic compliance	$7.76 \cdot 10^{-2}$
κ	elastic compliance	$8.40 \cdot 10^{-3}$
κ*	elastic compliance (strain)	$6.19 \cdot 10^{-3}$
ν	Poisson's ratio	0.3
λ*	elasto-viscoplastic compliance	$5.75 \cdot 10^{-2}$
M	CSL slope	1.33
μ*	creep index	$1.06 \cdot 10^{-3}$
OCR	apparent-OCR	1.34
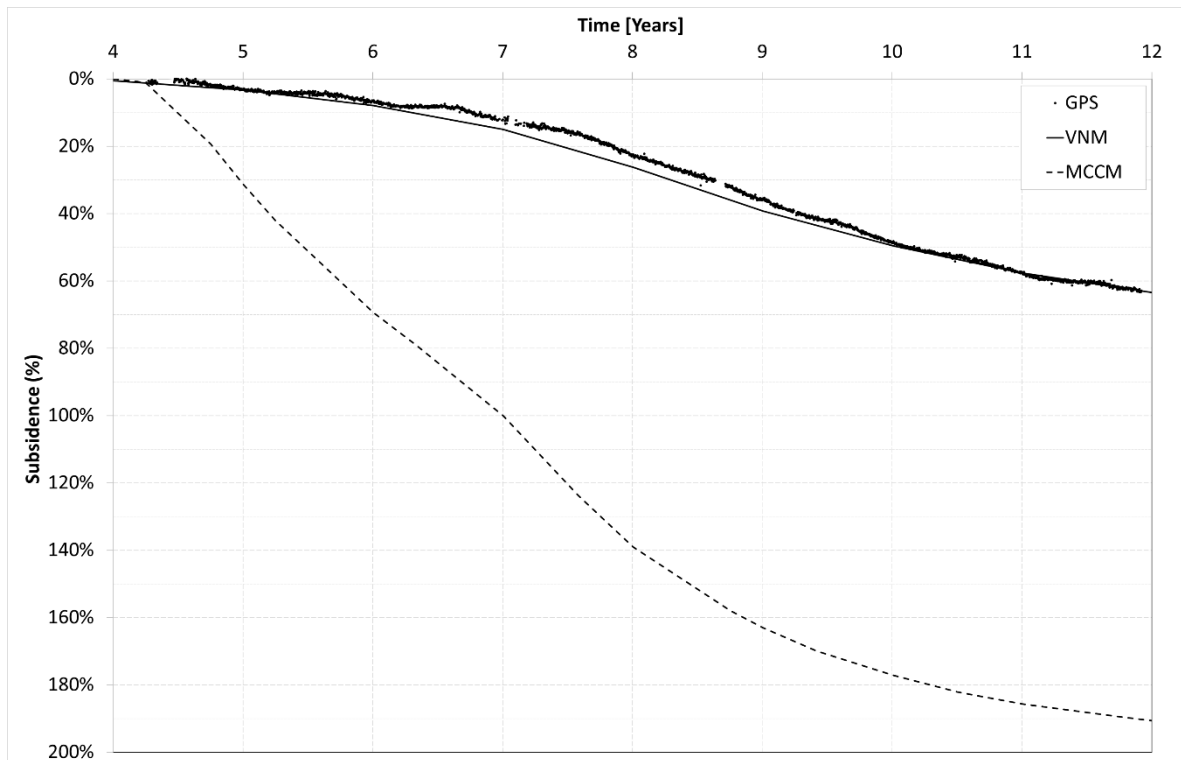
Fig. 15. Field 2: Comparison between evolution of measured and modelled vertical displacement in the period of GPS recording.

545
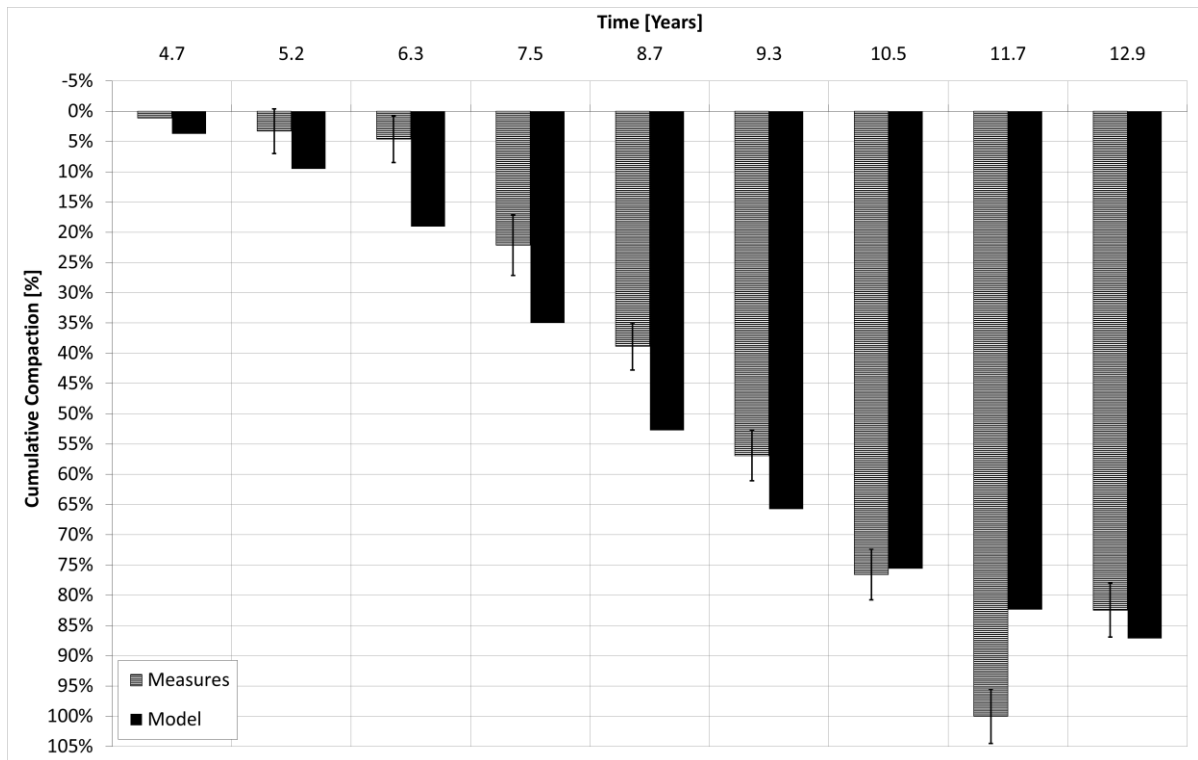
546   **Fig. 16.** Time evolution of compaction along the monitoring well of platform B (Field 2): markers data versus model

547   estimates.

548

549
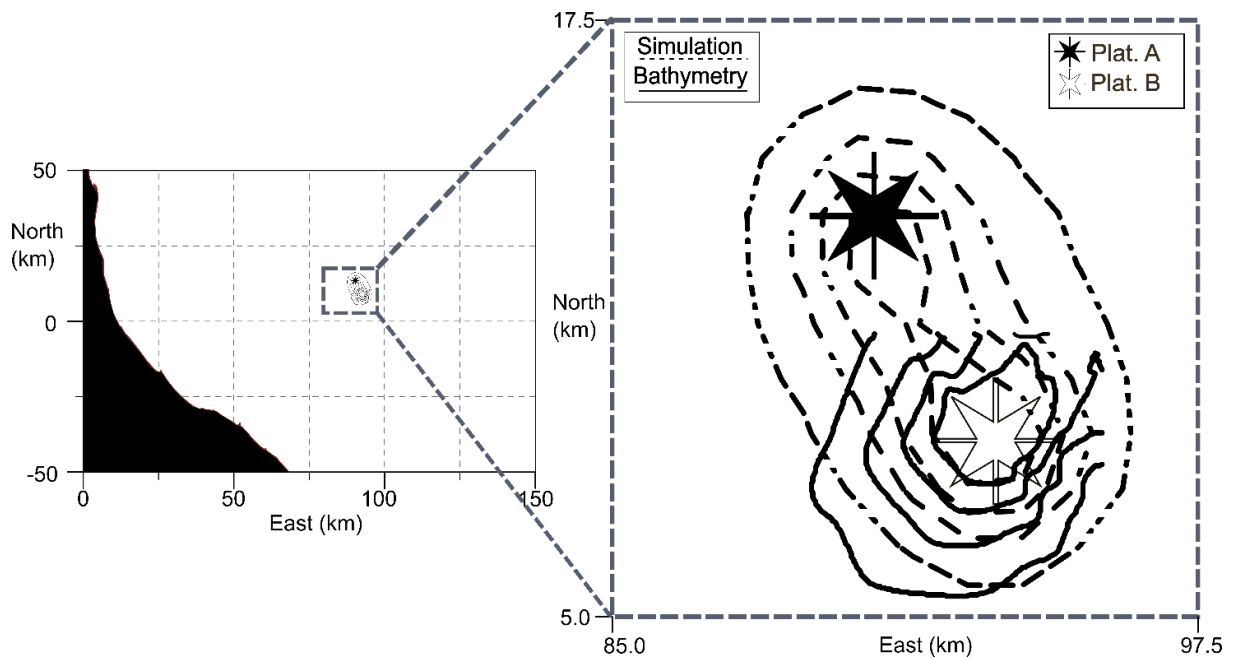
550   **Fig. 17.** Field 2: Contour lines (10%, 20%, 30% and 40%) of subsidence developed during the 7-year time interval

551   between the two bathymetric surveys: model estimates (dotted lines) versus measured data (solid lines).

552
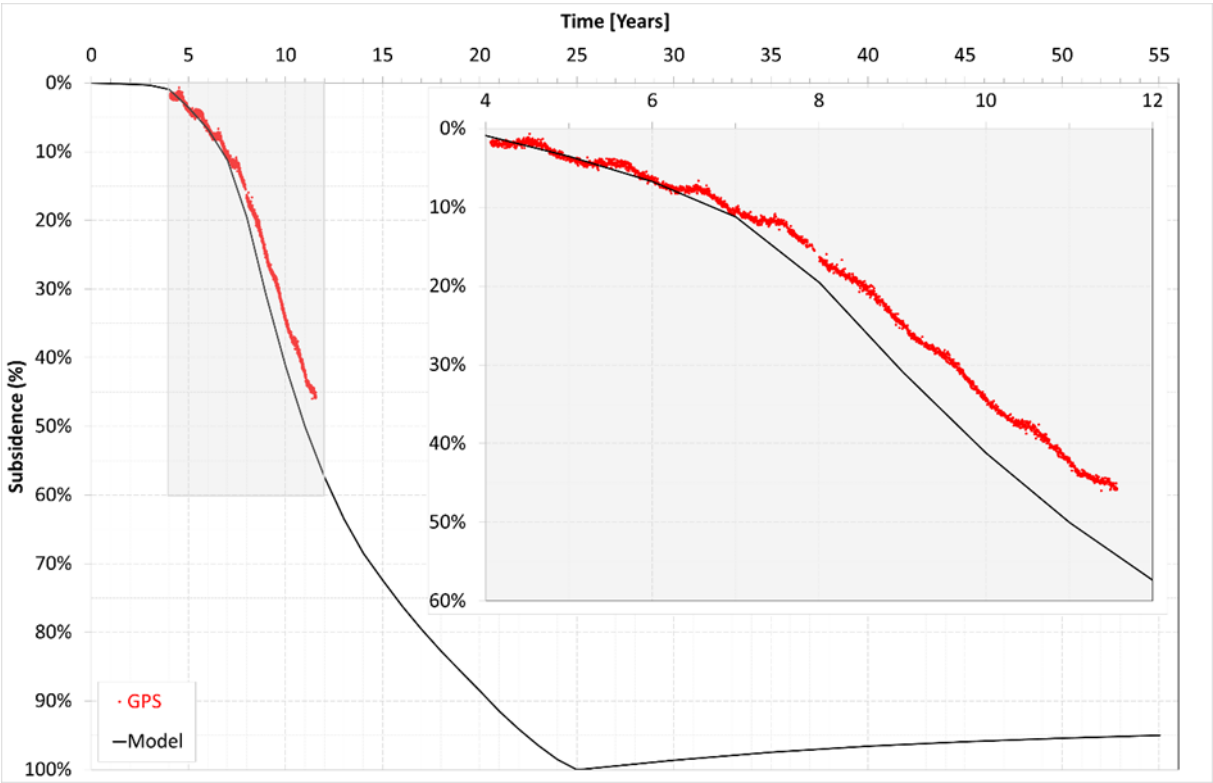
Fig. 18. Time evolution of subsidence at platform A: GPS data versus model estimate, with magnification.

555

556
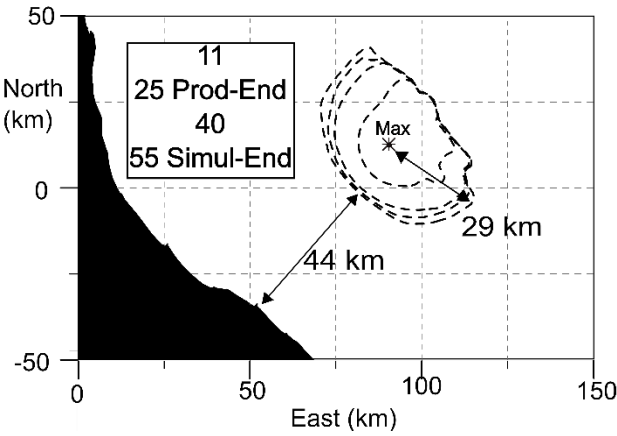
Fig. 19. Map with time evolution (after 11, 25, 40 and 55 years from start of production) of subsidence bowl extent. At

simulation end (30 years after the production-end), the subsidence bowl gets minimum distance from coastline and

maximum areal extent.

560

561 **5. Conclusions**

562 The evaluation and prediction of subsidence induced by hydrocarbon production is a complex task that involves advanced

563 monitoring and modeling techniques. The long time series of monitoring data currently available highlighted that, in many

564 cases, subsidence does not respond istantaneously to variations of fluids production rates. This 'delay' in subsidence

565 response could be captured by adopting 'time dependent' models to describe the mechanical behaviour of the geological

566 materials. Elasto-viscoplastic laws in the frame of the Overstress Theory offer a good compromise between simplicity

567 and accuracy when modeling time dependent behaviour. Among them, the Vermeer Neher model is of particular interest,

568 since model parameters can be derived from standard laboratory tests. The model was exploited to simulate the results of

569 laboratory tests done on samples of reservoir sands and silts from two gas reservoirs from the Adriatic Basin. It adequately

570 reproduced the main experimental outcomes, such as the dependency of the creep strain rates on the apparent OCR and

571 the reduced compressibility upon loading after creep. At regional scale, Finite Element simulations of the subsidence of

572 the two considered fields were also run using the VNM. A very good match of the monitoring data was obtained, both in

573 terms of maximum subsidence value and areal extent. Interestingly, this was achieved using the compliance and creep

574 parameters directly determined in the laboratory, while the apparent OCR was defined to be consistent with the geological

575 history of the basin.

576

579

580 **References**

581   1.   Dixon TH, Amelung F, Ferretti A, Novali F, Rocca F, Dokka R, et al.. Space geodesy: Subsidence and flooding

582   in New Orleans. *Nature*. 2006; 441(7093): 587–588.

583   2.   Chan FKS, Mitchell G, Adekola O, McDonald A. Flood risk in Asia's urban mega-deltas: Drivers, impacts and

584   response. *Environment and Urbanization ASIA*. 2012; 3(1): 41–61.

585   3.   Dijkema K. Impact Prognosis for Salt Marshes from Subsidence by Gas Extraction in the Wadden Sea. *Journal

586   of Coastal Research*. 1997; 13, 4: 1294-1304.

587   4.   Murria J. Subsidence Due to Oil Production in Western Venezuela: Engineering Problems and Solutions. In

588   *Land Subsidence (Proceedings of the Fourth International Symposium on Land Subsidence, May 1991)*. 1991.

589   IAHS Publ. no. 200:129-140.

590   5.   Takagi H, Fujii D, Esteban M, Yi X. Effectiveness and Limitation of Coastal Dykes in Jakarta: The Need for
591   Prioritizing Actions against Land Subsidence. *Sustainability*. 2017; 9, 619.

592   6.   Doornhof D, Kristiansen TG, Nagel NB, Pattilo PD, Sayers C. Compaction and Subsidence. *Oilfield Review*,
593   Autumn 2006; 50-68.

594   *7.*   Sulak RM. Ekofisk field: the first 20 years. *J. of Petroleum Technology, SPE, 43(10).* 1991; SPE Paper SPE-
595   20773-PA.

596   8.   Fjaer E, Holt RM, Raaen AM, Risnes R, Horsrud P. *Petroleum related rock mechanics*. 2nd ed. Development in
597   Petroleum Science, Vol. 53. Amsterdam, Holland: Elsevier; 2008.

598   9.   Kim J, Tchelepi HA, Juanes R. Stability, Accuracy, and Efficiency of Sequential Methods for Coupled Flow and
599   Geomechanics. Paper SPE-119084-PA. 2009.

600   10. Geertsma J. Problems of rock mechanics in Petroleum Production Engineering. *Proceedings of the First*
601   *Congress of the International Society of Rock Mechanics*. 1966; 585-584

602   11. Geertsma J. Land Subsidence Above Compacting Oil and Gas Reservoirs. *Journal of Petroleum Technology*.
603   1973; 25: 06.

604   12. Mehrabian A, Abousleiman N. Geertsma's subsidence solution extended to layered stratigraphy. *Journal of*
605   *Petroleum Science and Engineering*. 2015; 130: 68-76.

606   13. Tempone P, Fjær E, Landrø M. Improved solution of displacements due to a compacting reservoir over a rigid
607   basement. Applied Mathematical Modelling. 2010; 34: 3352- 3362.

608   14. Roscoe K, Burland JB. On the generalized stress-strain behaviour of wet clay. *Engineering Plasticity*. 1968.
609   Cambridge Univ. Press, 535-609

610   15. Abdulraheem A, Zaman M, Roegiers JC. A finite-element model for Ekofisk field subsidence. *Journal of*
611   *Petroleum Science and Engineering* 1994; 10 (4); 299-310.

612   16. Capasso G, Mantica S. Numerical simulation of compaction and subsidence using Abaqus. *Proc. Abaqus Users'*
613   *Conference,* Boston (USA). 2006: 125-144.

614   17. Gemelli F, Monaco S, Mantica S. Modelling methodology for the analysis of subsidence induced by exploitation
615   of gas fields. *Proc. Second EAGE Workshop on Geomechanics and Energy, Celle (Germany)*. 2015.. cp-466-
616   00001.

617   18. van Thienen-Visser K, Breunese JN, Muntendam-Bos AG. Subsidence due to gas production in the Wadden
618   Sea: How to ensure no harm will be done to nature. *49th US Rock Mechanics / Geomechanics Symposium held*
619   *in San Francisco*, CA, USA, 28 June-1 July 2015.

19. Morton RA, Bernier JC. Recent subsidence-rate reductions in the Mississippi Delta and their geological implications. *Journal of Coastal Research.* 2010; 26, 3: 555–561.

20. Chang C, Mallman E, Zoback M. Time-dependent subsidence associated with drainage induced compaction in Gulf of Mexico shales bounding a severely depleted gas reservoir. *AAPG Bulletin.* 2014; 98, 6: 1145–1159

21. Gemelli F, Corradi A, Volonté G, Mantica S, De Simoni M. Elasto-viscoplastic modeling of subsidence above gas fields in the Adriatic Sea. *Proceedings of the International Association of Hydrological Sciences.* 2020; 382:463.

22. Mossop A. An explanation for anomalous time dependent subsidence. *46th U.S. Rock Mechanics/Geomechanics Symposium, 24-27 June, Chicago, Illinois* 2012. Paper ARMA 2012-518

23. Hettema M, Papamichos E, Schutjens PMTM. Subsidence delay: field observations and analysis. *Oil & Gas Science and Technology.* 2002; 57(5): 443-458

24. Mesri G. Coefficient of secondary compression. J. *Soil Mech. Found. Div.*, *ASCE.* 1973; 99 (1): 123-137.

25. Mesri G, Godlewski PM. Time and stress-compressibility interrelationship. *J. Geotech. Eng.* 1977; 103(5): 417-430.

26. Hagin PN, Zoback MD. Viscous deformation of unconsolidated sands – Part 1: Time-dependent deformation, frequency dispersion, and attenuation. *Geophysics.* 2004; 69, 3: 732-741.

27. Chang C, Zoback MD. Viscous creep in room-dried unconsolidated Gulf of Mexico shale (I): Experimental results. *Journal of Petroleum Science and Engineering.* 2009; 69: 239-246

28. Voyiadjis G Y, Zhou Y. Time-dependent modeling of subsidence due to drainage in bounding shales: Application to a depleted gas field in Louisiana. *Journal of Petroleum Science and Engineering.* 2018; 166: 175-187.

29. Vermeer PA, Neher HP. A soft soil model that accounts for creep. In *Proc. Int. Symp. "Beyond 2000 in Computational Geotechnics".* 1999; 249-261, Balkema, Rotterdam.

30. Liingaard M, Augustesen A, Lade PV. Characterization of models for time-dependent behavior of soils. *Int. Journal of Geomechanics.* 2004; 4, 2: 157–177.

31. Naghdi PM, Murch SA. On the mechanical behavior of viscoelastic/plastic solids. *J. Appl. Meteorol.* 1963; 30: 321–328.

32. Olszak W, Perzyna P. Stationary and nonstationary viscoplasticity. 1970. McGraw-Hill, New York.

33. Šuklje L. The analysis of the consolidation process by the isotache method. *In: Proc. 4th Int. Conf. on Soil Mech. and Found. Engng., London.* 1957; 1:200–6.

650   34. De Gennaro V, Pereira JM. A viscoplastic constitutive model for unsaturated geomaterials. *Computer and*

651   *Geotechnics*. 2013; 54:143–51.

652   35. Leroueil S, Kabbaj M, Tavenas F, Bouchard R. Stress strain-strain rate relation for the compressibility of

653   sensitive natural clays. *Géotechnique.* 1985; 35 (2): 159–180.

654   36. de Waal J, Smits R. Prediction of reservoir compaction and surface subsidence: field application of a new model.

655   *SPE Form Eval.* 198; 83:347–56.

656   37. Cassiani G, Brovelli A, Hueckel T. A strain-rate-dependent modified Cam-Clay model for the simulation of

657   soil/rock compaction. *Geomechanics for Energy and the Environment* 2017; 11:42-51.

658   38. Qiao Y, Ferrari A, Laloui L, Ding W. Nonstationary flow surface theory for modeling the viscoplastic behaviors

659   of soils. *Computers and Geotechnics*. 2016; 76: 105-119.

660   39. Alonso EE, Gens A, Josa A. A constitutive model for partially saturated soils. *Géotechnique* 1990; 40(3):405–

661   30.

662   40. Malvern LE. The propagation of longitudinal waves of plastic deformation in a bar of metal exhibiting a strain

663   rate effect. *J. Appl. Mech..* 1951; 18: 203–208.

664   41. Perzyna P. The constitutive equations for rate sensitive plastic materials. *Q. Appl. Math.* 1963; 20, 4: 321–332.

665   42. Perzyna P. Fundamental problems in viscoplasticity. *Advances in Applied Mechanics.* 1966; 9: 243–377.

666   43. Yin Z-Y, Chang CS, Karstunen M, Hicher PY. An anisotropic elastic–viscoplastic model for soft clays.

667   *International Journal of Solids and Structures*. 2010; 47, 5: 665-677.

668   44. Kutter BL, Sathialingam N. Elastic–viscoplastic modelling of the ratedependent behaviour of clays.

669   *Géotechnique.* 1992; 42 (3): 427–441.

670   45. Yin JH, Zhu JG, Graham J. A new elastic–viscoplastic model for time dependent behaviour of normally and

671   overconsolidated clays: theory and verification. *Canadian Geotechnical Journal.* 2002; 39 (1): 157–173.

672   46. Hickman RJ, Gutierrez MS. Formulation of a three dimensional rate dependent constitutive model for chalk and

673   porous rocks. *Int. J. of Numerical and Anal. Meth. in Geomechanics*. 2006; 31 (4): 583-605.

674   47. Leoni M, Karstunen M, Vermeer PA. Anisotropic creep model for soft soils. *Géotechnique*. 2008; 58 (3): 215–

675   226.

676   48. Hueckel T, Cassiani G, Tao F, Pellegrino A, Fioravante V. Aging of oil/gas-bearing sediments, their

677   compressibility and subsidence. *Journal of Geotechnical and Geoenvironmental Engineering*. 2001; 127, 11:

678   926 – 938.

679   49. Leonards GA, Altschaeffl AG. Compressibility of clay. *J. Soil Mech. and Found. Div.*, *ASCE.* 1964; 90(5): 133–

680   155.

681   50. Bjerrum L. Embankments on soft ground. *Proc. of ASCE Spec. Conf. on Performance of earth and earth*

682   *supported structures* 1972; 2: 1–54.

683   51. Bjerrum L. Problems of soil mechanics and construction on soft clays. *8th International Congress of Soil*

684   *Mechanics and Foundation Engineering* 1973; 3: 111–159.

685   52. Mesri G, Feng TW, Benak JM. Postdensification penetration resistance of clean sands. *J. Geotech. Engrg.,*

686   *ASCE*. 1990; 116(7): 1095–1115.

687   53. Schmertmann JH. The mechanical aging of soils. *J. Geotech. Engrg., ASCE*. 1991; 117(9): 1288–1330.

688   54. Brignoli M, Fanuel P, Holt RM, Kenter CJ. Effects on core quality of a bias stress applied during coring.

689   *SPE/ISRM Eurock 98, Trondheim (Norway)*. 1998; SPE47262.

690   55. Pemper R, Fjell L, Gold R. Field examples with a new compaction monitoring instrument. *38th SPWLA Annual*

691   *Logging Symposium, June 15-18, Houston, Texas.* 1997; SPWLA-1997-MM.

692   56. Macini P, Mesini E. Radioactive markers technique application to evaluate compaction in environmentally

693   sensitive areas. *SPE international petroleum conference and exibition. February 10-12, Villahermosa, Mexico.*

694   2002*; SPE74411.*

695   57. Nguyen SK, Volonté G, Musso G, Brignoli M, Gemelli F, Mantica S. Implementation of an elasto-viscoplastic

696   constitutive law in Abaqus/Standard for an improved characterization of rock materials. *Abaqus Users'*

697   *Conference, Boston (USA), Natural Resources*. 2016; 710: 710–724.

698   58. Cremonesi M, Ghisi A, Perego U, Corradi A, Gemelli F, Mantica S. A Numerical Study on Explicit vs Implicit

699   Time Integration of the Vermeer-Neher Constitutive Model. In: Carcaterra A, Paolone A, Graziani G, eds.

700   *Proceedings of XXIV AIMETA Conference 2019*. AIMETA 2019.

701   59. Della Vecchia G, Pandolfi A, Musso G, Capasso G. An analytical expression for the determination of in situ

702   stress state from borehole data accounting for breakout size. *International Journal of Rock Mechanics and*

703   *Mining Sciences.* 2014; 66, 64-68, ISSN 1365-1609.

704   60. Scelsi G, De Bellis ML, Pandolfi A, Musso G, Della Vecchia G. A step-by-step analytical procedure to estimate

705   the in-situ stress state from borehole data. *Journal of Petroleum Science and Engineering*. 2019; 176: 994-1007.